Master's thesis

NTNU
Norwegian University of Science and Technology
Faculty of Engineering
Department of Energy and Process Engineering

Ingelin Herland

Design-Optimization of a Francis turbine draft tube

Master's thesis in Energy and Environmental Engineering
Supervisor: Bjørn Winther Solemslie
June 2020

NTNU
Norwegian University of
Science and Technology

Ingelin Herland

Design-Optimization of a Francis turbine draft tube

Master's thesis in Energy and Environmental Engineering
Supervisor: Bjørn Winther Solemslie
June 2020

Norwegian University of Science and Technology
Faculty of Engineering
Department of Energy and Process Engineering

Ingelin Herland

Design-optimization of a Francis turbine draft tube

Thesis for the degree of Master of Science

Trondheim, June 2020

Norwegian University of Science and Technology
Faculty of Engineering Science and Technology
Department of Energy and Process Engineering

NTNU
Innovation and Creativity

Dedicated to

Moffa

Norwegian University of Science and Technology

Faculty of Engineering
Department of Energy and Process Engineering

NTNU

MASTER THESIS
for
student Ingelin Herland
Spring 2020

Design-optimization of a Francis turbine draft tube
Optimalisering av sugerøret til en Francis turbin

Background

The contemporary electricity market demands a robust mechanism that allows integration of various sources of energy. Power produced from intermittent energy sources, such as wind energy and solar energy, fluctuates. This means that other generating units need to absorb the fluctuations (known as short peaks). Hydraulic turbines are extensively used to absorb the short peaks. The number of short peaks and the ramping have increased tenfold in the last two decades. Such high numbers of ramping have pushed the hydraulic turbines to the endurance limit, and the turbines have started to show signs of fatigue. Studies in recent years have clearly indicated that the increased numbers of ramping, including load variation, start-stop, total load rejection and speed-no-load, affect the expected life of the turbines. Therefore, understanding the mechanical behavior of turbine blades under different operating conditions is essential for future design of the turbine. Existing turbine design have certain limitations and is not profitable in the variable electricity market.

Project work is the part of on-going research activities in the Waterpower Laboratory, Department of Energy and Process Engineering, NTNU. Student will collaborate with on-going research under H2020-HydroFlex-WP3 (www.h2020hydroflex.eu) project. The focus will be optimization of draft tube under variable-speed operating condition. Large scale design optimization are carrying out in the laboratory. The student will use newly optimized runner design to improve the existing draft tube design.

Objective

Design and optimization of a high head Francis turbine draft tube for variable-speed turbine operation. Focus will be steady state operating conditions of the turbine.

The following tasks are to be considered:

1. Literature study
    a. Francis turbines and design of draft tubes
2. Software knowledge
    a. CAD-drawing by CREO and ANSYS CFX
3. CFD-analysis
    a. Runner
    b. Draft tube with and without runner domain
    c. Validation of the assumption of enforced boundary condition when simulating draft tube volume without runner
    d. Investigate optimization of draft tube for variable speed operation
4. Evaluation of the numerical results
5. If the student is going to Nepal on an excursion, the previous work from the project and the further work in this master thesis will be written as a separate publication and presented at the conference:10th International symposium on Current Research in Hydraulic Turbines (CRHT-X) at Kathmandu University 31st March 2020.

Address
N-7034 Trondheim
Norway

Location
K. Hejes vei 1b

Tel. +47 73 59 38 60
Fax +47 73 59 35 80
Org. no. NO 974 767 880

-- “ --

The work shall be edited as a scientific report, including a table of contents, a summary in Norwegian, conclusion, an index of literature etc. When writing the report, the candidate must emphasise a clearly arranged and well-written text. To facilitate the reading of the report, it is important that references for corresponding text, tables and figures are clearly stated both places.
By the evaluation of the work the following will be greatly emphasised: The results should be thoroughly treated, presented in clearly arranged tables and/or graphics and discussed in detail.

The candidate is responsible for keeping contact with the subject teacher and teaching supervisors.

Risk assessment of the candidate's work shall be carried out according to the department's procedures. The risk assessment must be documented and included as part of the final report. Events related to the candidate's work adversely affecting the health, safety or security, must be documented and included as part of the final report. If the documentation on risk assessment represents a large number of pages, the full version is to be submitted electronically to the supervisor and an excerpt is included in the report.

According to “Utfyllende regler til studieforskriften for teknologistudiet/sivilingeniørstudiet ved NTNU” § 20, the Department of Energy and Process Engineering reserves all rights to use the results and data for lectures, research and future publications.

Submission deadline: 10.June 2020

☐ Work to be done in the Waterpower laboratory
☐ Field work

Department for Energy and Process Engineering, *10. January 2020*

Bjørn Winther Solemslie
Supervisor

Co-Supervisor(s): Igor Iliev
Erik Tengs
Ole Gunnar Dahlhaug

Preface

This thesis is a result of the authors work as a Master student at the Waterpower Laboratory, Depeartment of Energy and Process Engineering (EPT) at the Norwegian University of Science and Technology (NTNU) in Trondheim, Norway. The work has been a collaboration with on-going research under H2020-HydroFlex-WP3 project organized by HydroCen. Two weeks were spent at EDR Medeso's office to develop expertise with the software ANSYS.

WATERPOWER LABORATORY

NTNU

Abstract

This thesis documents optimization of the draft tube designs to Francis turbine operating at variable speed. Optimal designs are discussed in terms of increased pressure recovery and decreased volume, relative to a reference design. Three operation points corresponding to part load, best efficiency point, and high load operating conditions are considered for the analysis.

The draft tube geometry is constructed as a function of 11 design variables. Box-Behnken design is used to provide design samples, which in turn are evaluated by computational fluid dynamics simulations. The simulations calculate the optimization objectives, which are the pressure recovery factor at different operation points and the draft tube volume. The simulated objective values are utilized for building response surfaces in MATLAB, which in turn, are used to predict responses for new designs.

$100 \cdot 10^6$ random designs were evaluated by the response surfaces, where $10.2 \cdot 10^6$ designs were found to give equal or better performance across all four objectives. 5 optimized designs were suggested; the first 4 corresponding to designs with the highest given score for a single objective, while at the same time being at least as good as the reference across the remaining three. The last proposed design was selected by considering simultaneous improvement across all 4 objectives.

The predicted responses of the suggested designs were verified against simulations. The results showed substantial improvements for all designs, except the design favoring decreased draft tube volume. The pressure recovery of this design was predicted to be at least as good as the reference, but simulation results for part load and best efficiency point operating conditions showed small degradations. Part load results showed higher uncertainty than the other operating conditions. Despite potential errors in simulations and predictions, improved designs were found, demonstrating that the optimization method works.

Sammendrag

Denne masteroppgaven omhandler optimalisering av sugerøret til en Francisturbin som opererer på variabelt turtall. Forbedrede design er diskutert relativt et referansedesign, i form av økt trykkgjenvinning gjennom sugerøret og redusert volum. Analysen er begrenset til å optimere sugerøret for tre ulike driftspunkt, henholdsvis lav last, best punkt og høy last.

Sugerørsgeometrien er konstruert som en funksjon av 11 ulike variabler. Box-Behnken Design er benyttet til å gjøre et utvalg av design som videre er evaluert med CFD-simuleringer i ANSYS CFX. Simuleringene regner ut optimeringsobjektivene, som er trykkgjenvinningskoeffisienten ved de tre driftspunktene og volumet av sugerøret. Disse verdiene benyttes til å bygge respons overflater for hvert objektiv i MATLAB, som videre predikerer responsen av nye design.

$100 \cdot 10^6$ tilfeldige design er evaluert av respons overflatene, der $10.2 \cdot 10^6$ design er predikert til å være like gode eller bedre enn referansedesignet for alle objektivene. Blant denne mengden er 5 optimaliserte design foreslått, hvorav 4 maksimerer hvert objektiv enkeltvis, mens det siste vekter en samlet forbedring av alle objektivene.

Den predikerte responsen av de foreslåtte designene er verifisert med CFD- simuleringer. Alle designene viser forbedringer i alle objektiver, med unntak av designet som vekter reduksjon av sugerørsvolumet. Trykkgjenvinningskoeffisientene er predikert til å være forbedret, men simuleringer på driftspunktene lav last og best punkt gir resultater like under referanseverdiene. Generelt viser lav last en gjennomgående høyere usikkerhet i analysen, sammenlignet med de andre driftspunktene. Til tross for potensielle usikkerhetsmomenter i simuleringer og predikasjoner, er forbedrede design blitt predikert og verifisert. Dette demonstrerer at optimeringsmetoden fungerer.

Acknowledgements

I would like to express my gratitude to my supervisor Bjørn Winther Solemslie. Thank you for all the wise thoughts you have shared. I think you should reconsider your usual end-remark whenever helping me out with the thesis: "Det var da så lite". Your help is way more valuable than that!

My co-supervisors Igor Iliev and Erik Tengs also deserve a big honor. Igor, you have been such a great help several ways. From being an optimization oracle, helping me break down my problem into understandable pieces, to ensuring power supply for my computer. Thank you for guiding me through this thesis. As for Erik, I would like to thank you for answering all my CFD questions seriously, even though some of them probably were quite silly.

I would like to thank all my supervisors for being available despite the sudden shut down of the world that occurred this spring. Whenever I got lost, help was only a Teams call away.

This thesis was kick-started with a two-week bootcamp, getting into the CFD world of ANSYS at EDR Medeso's office. I would like to thank Ole Gunnnar Dalhaug for making this arrangement possible. Also, I would like to thank all the employees at EDR Medeso for being friendly and helpful. A special thanks goes to Flora Charrassier, the Scripting Queen of ANSYS SpaceClaim and to Maria Rolstad Jordal for helping me whenever I encountered a problem.

I would also like to thank all the Master Students and PhD-Candidates at the Waterpower Laboratory for contributing to a social and fun working environment. It has been a pleasure sharing my time with you this year!

My family, friends and housemates; thank you for all being my cheerleaders. A special thanks goes to Moffa, my grandfather, for all support and emails throughout my five years at NTNU. Thank you!

Contents

List of Tables

List of Figures

List of Symbols

Latin Symbols

C_p	Pressure Recovery Factor	$-$
V	Draft tube volume	m^3
c	Absolute velocity	$^{\mathrm{m}}/_{\mathrm{s}}$
u	Peripheral velocity	$^{\mathrm{m}}/_{\mathrm{s}}$
w	Relative velocity	$^{\mathrm{m}}/_{\mathrm{s}}$
A	Area	m^2
g	Gravitational acceleration	$^{\mathrm{m}}/_{\mathrm{s}^2}$
H	Available head	m
h	Hydraulic losses	m
H_R	Useful head	m
p	Pressure, number of regression coefficients	$Pa, -$
Q	Discharge	$^{\mathrm{m}^3}/_{\mathrm{s}}$
E	Actual total flow energy	m
$E_{k,Q}$	Discharged-averaged kinetic flow energy	m
E_k	Actual kinetic flow energy	m
E_Q	Discharged-averaged total flow energy	m

k	Kinetic energy of the turbulence	$\mathrm{m}^2/\mathrm{s}^2$
Re	Reynolds number	$-$
u_τ	Friction velocity	m/s
y^+	Dimensionless wall distance	$-$
$\hat{y}$	Response prediction	$-$
m	Number of samplings	$-$
n	Number of design variables	$-$
R^2_{adj}	Adjusted R-square coefficient	$-$
x_i	Design parameter	$-$
d_2	Geometric parameter of the cone outlet diameter	m
d_3	Geometric parameter of the diameter of the elbow outlet	m
h_1	Geometric parameter of the cone height	m
L	Geometric parameter of the horizontal length of the draft tube	m
l_1	Geometric parameter of the horizontal length of the elbow	m
l_2	Geometric parameter of the vertical length of the elbow	m
l_3	Geometric parameter of the length of the elbow outlet	m
l_4	Geometric parameter of the height of the draft tube outlet	m
l_5	Geometric parameter of the width of the draft tube outlet	m
r_1	Geometric parameter of the radius of the draft tube outlet corners	m

Greek Symbols

η_h	Hydraulic efficiency	$-$
η_{C_p}	Draft tube efficiency	$-$
μ	Dynamic viscosity	$Pa \cdot s$
ν	Kinematic viscosity	m^2/s
ρ	Density	kg/m^3

τ_w	Wall shear stress	Pa
ξ	Energy Loss Coefficient	$-$
ϵ	Error, Energy dissipation rate	$\%, \mathrm{m}^2/\mathrm{s}^2$
β	Regression coefficient	$-$
σ_e	Root Mean Square Error	$-$
α	Geometric parameter of the exit diffuser pitch	$^\circ$

Abbreviation

BC	Boundary Condition
BEP	Best Efficiency Point
BL	Boundary Layer
CFD	Computational Fluid Dynamics
CEL	CFX Expression Language
CV	Center Value
DP	Design Point
DT	Draft Tube
DV	Design Variable
FS	Full Simulation
GP	Geometric Parameter
HL	High Load
LL	Lower Limit
M	Million
NTNU	Norwegian University of Science and Technology
OP	Operation Point
PIMP	Predicted Improved Modeled Population
PL	Part Load

PS	Partial Simulation
RMS	Root Mean Square
RANS	Reynolds Averaged Navier-Stokes
RSM	Response Surface Modeling
SBO	Surrogate-based Optimization
UL	Upper Limit
VSO	Variable Speed Operation

Indices

$*$	Condition at Best Efficiency Point
0	Position indication, stay vane inlet
1	Position indication, draft tube inlet
2	Position indication, draft tube outlet
i	Interface location, design variable
ref	Reference draft tube design

Chapter I

Introduction

■ This chapter gives an introduction to the thesis. The first section explains hydropower plants' role in the energy market, the draft tubes importance, and the motivation behind variable speed operation. The second section quantifies the objective and the limitations of the thesis. The final section describes the thesis outline.

1.1 Background and motivation

Hydropower is the primary source of electricity in Norway, and it contributed to 95% of the domestic power production in 2018 [7]. Among the various types of turbines, 60% of the global hydropower capacity is covered by Francis turbines [8]. Francis turbines are also the most utilized type of turbine in Norway [9].

The draft tube (DT) is located after the runner of a Francis turbine. Its main task is to convert kinetic energy of the water leaving the runner into pressure energy. The pressure recovery in the DT increases the transferred energy into the runner. Hence, the performance of the DT affects the efficiency of the hydropower plant.

Energy production from solar and wind highly depends on weather conditions. This leads to unpredictable power production, which creates fluctuations in the electricity market. These fluctuations are expected to increase, whereas power production from wind and solar would be more present in the future energy mix [10].

Hydropower has the advantage of robust power supply and adjustability. Thus, hydropower plants are expected to dampen the fluctuations in the electricity marked.

As a consequence, hydropower plants are commonly operated at other discharges than their best efficiency point (BEP), introducing additional losses. Variable speed operation (VSO) of the runner has been suggested by several studies as a measure to improve efficiency at off-design operating conditions [11]. However, VSO introduces another flow condition in the DT. Consequently, improved hydropower plant efficiency may be attainable by optimization of the DT for VSO.

1.2 Objective and limitations

The main objective of this master thesis is defined as:

Design and optimization of a high head Francis turbine draft tube for variable-speed turbine operation. Focus will be steady-state operating conditions of the turbine.

The work is part of on-going research activities in the Waterpower Laboratory at NTNU related to the HydroFlex research-project organized by HydroCen [12]. A newly optimized runner design for VSO has been developed as part of this research, and is utilized for providing operating conditions for the DT optimization work.

As a starting point for the optimization, a scaled version of the DT in Tokke power plant in Norway is utilized. This is the draft tube utilized in the Francis-99 research project [13], and a physical model of the DT exists in the Waterpower Laboratory at NTNU.

The optimization is performed with computational fluid dynamics (CFD) analysis of a parametric DT design. The optimal DT design is discussed in terms of achieving high pressure recovery and small volume.

Available Computational resources and time put restrictions on the work presented in this thesis. The analysis is limited to a discussion around design optimization of 3 operation points (OP); Part Load (PL), BEP, and High Load (HL). The simulations run on a relatively coarse mesh, and turbulence is modeled with the $k - \epsilon$ model. Transient effects are neglected from the analysis as all simulations are modeled as steady-state. The presence of possible cavitation is not considered.

1.3 Outline

The thesis is structured in 6 chapters, following this introduction. Chapter 2 explains relevant theory about hydropower plants, optimization and CFD modeling. Chapter 3 lists previous work related to design development of DTs. The method of the optimization is presented in Chapter 4, as well as tests performed to investigate numerical accuracy and potential modeling errors introduced by the boundary con-

ditions (BCs). The results of the optimization and additional tests are displayed in Chapter 5. Chapter 6 discusses optimal designs and uncertainties. Finally, Chapter 7 concludes on whether optimal designs for the three considered OPs were found and propose avenues for future research.

The Francis 99 DT is hereby referred to as $\mathrm{DT}_{Francis\,99}$ throughout the thesis. The VSO runner utilized for the analysis is referred to as the runner.

Symbols and abbreviations are only defined the first time they are mentioned in the text, but an overview is listed in the nomenclature. Several abbreviations and index notations are utilized to more compactly describe the different types of simulations performed. This scheme will be further outlined with the methodology in Chapter 4.

To make the thesis more readable, references used throughout entire sections or chapters will only be cited once at the beginning of the respective body of text.

Chapter II

Theory

■ This chapter is divided into three main sections. The first presents theory about hydropower plants and draft tubes, the second presents CFD theory, and the last presents optimization theory using surrogate models.

2.1 Hydropower plants

Hydropower plants convert potential energy of stored water into electricity. There exist various types of turbines, which in general belong to two main groups: impulse turbines and reaction turbines. In reaction turbines, both kinetic and pressure energy in the water is converted into mechanical work in the runner. Francis turbines belong to this category.

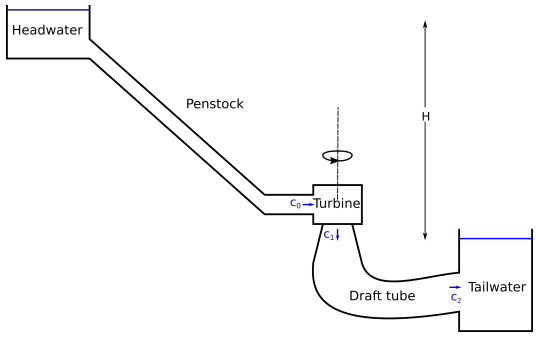

Figure 2.1: Sketch of a hydropower plant with a Francis Turbine. Water is entering the runner in the tangential direction and leaving in the axial direction, relative the rotation axis.

The water is directed to the Francis turbine from the headwater through the penstock, as seen in figure 3.1. It then flows through the runner and is discharged through the DT into the tailwater. The DT's main task is to convert kinetic energy at the outlet of the runner into pressure energy at the outlet of the DT. Additional advantages of the DT are that it enables placing the runner above the tailwater without losing any head. However, placing the runner too high above the tailwater is not desirable, as it increases the risk of cavitation. The DT increases the overall efficiency of the hydropower plant as illustrated in figure 2.2.

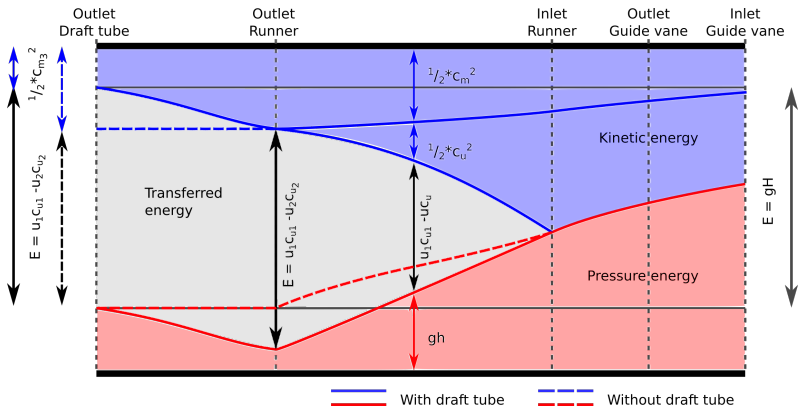

Figure 2.2: Specific energy conversion in a Francis turbine. c_m denotes water velocity in the meridian direction, as c_u denotes water velocity in the tangential direction of the runner.

Water enters the inlet of the runner with both kinetic- and pressure energy, which both contribute to power production. The remaining kinetic energy in the water at the outlet of the runner is considered as losses. However, it can be utilized by converting it into pressure energy with the DT. The tailwater bounds the pressure at the outlet of the DT. Thus, pressure recovery throughout the DT decreases the pressure at the outlet of the runner. Hence, the total energy converted to the rotational energy of the runner will increase.

Low head reaction turbines are characterized by a higher fraction of kinetic- relative pressure energy in the water. Thus, kinetic energy losses are more present, and pressure recovery in the DT becomes more substantial for turbine efficiency.

2.1.1 Variable speed operation

Traditionally, Francis runners operate at synchronous speed. The historical reason is that generators require a specific rotational speed of the runner to produce electricity with the correct frequency for the electrical grid.

Turbines are designed for operating at BEP, where the hydropower plant efficiency is highest, and discharge is denoted Q^*. The discharge regulates produced power. At PL operating conditions, $Q < Q^*$ and less power is produced compared to BEP. In contrast, when operating at HL, $Q > Q^*$ and more power is produced. However, two significant losses reduce the turbine efficiency when operating at off-design conditions: incidence losses at the inlet of the runner and swirl losses at the outlet of the runner. By introducing VSO of the turbine, these losses are reduced by adjusting the runner speed. Hence, the power production is regulated by both runner speed and discharge, which increase efficiency when operating at off-design conditions.

Notably, VSO requires additional frequency adjustments of the generated power, before transmission into the electrical grid. Two frequently used methods for achieving this are Full Size Frequency Converters and Doubly-Fed Induction Machines [14]. Both techniques introduce additional losses, compared to operating at synchronous speed.

2.1.2 Relating draft tube losses to turbine efficiency

The following section and subsection 2.1.3 is based on the theory given in Lyutov 2015 [15].

Index i of the variables refer to locations in the hydropower plant. Index 0 denotes the inlet of the stay vanes, index 1 denotes the runner-DT interface, and index 2 denotes the DT outlet. The index locations are illustrated with the absolute velocity c in Figure 3.1.

The hydraulic efficiency η_h of a hydropower plant turbine is defined as:

$$\eta_h = \frac{H_R}{H} \tag{2.1}$$

H_R is the useful head converted into power, and H is the available head. By definition, H denotes the difference in total head between the entrance of the spiral casing to the outlet of the DT.

$$H = E_{Q,0} - E_{Q,2} \tag{2.2}$$

$E_{Q,i} = p_i/\rho g + z_i + c_i^2/2g$ is the discharged averaged head at interface i. p denotes pressure, g is the gravity constant and z potential height. p_i and c_i are further defined as:

$$p_i = \frac{1}{Q}\iint_{A_i} p(\boldsymbol{c}\cdot d\boldsymbol{A}) \tag{2.3}$$

$$c_i = \frac{1}{A_i}\iint_{A_i} \boldsymbol{c}\cdot d\boldsymbol{A} = Q/A_i \tag{2.4}$$

To better understand the energy conservation in a hydropower plant, three fluxes, namely the actual total flow energy E_i, the actual kinetic flow energy $E_{k,i}$ and the discharged-based kinetic flow energy $E_{k,Q,i}$, are defined for interface $i = 0, 1, 2$.

$$E_i = \frac{1}{Q}\iint_{A_i}\left(\frac{p}{\rho g} + z + \frac{\boldsymbol{c}^2}{2g}\right)(\boldsymbol{c}\cdot d\boldsymbol{A}) \tag{2.5}$$

$$E_{k,i} = \frac{1}{Q}\iint_{A_i}\frac{\boldsymbol{c}^2}{2g}(\boldsymbol{c}\cdot d\boldsymbol{A}) \tag{2.6}$$

$$E_{k,Q,i} = \frac{1}{Q}\iint_{A_i}\frac{Q^2}{2gA_i^2}(\boldsymbol{c}\cdot d\boldsymbol{A}) = \frac{Q^2}{2gA_i^2} \tag{2.7}$$

The flow at the inlet of the spiral casing is approximately uniform over the section, which gives $E_0 \approx E_{Q,0}$. In contrast, the flow at the outlet of the DT is not uniform, which gives rise to the outlet losses, h_{out}.

$$h_{out} = E_2 - E_{Q,2} = E_{k,2} - E_{k,Q,2} \tag{2.8}$$

The hydraulic losses, h_{DT} in the DT, define the change in flow energy throughout it.

$$h_{DT} = E_2 - E_1 \tag{2.9}$$

Additionally, the flow will have losses related to interaction with the spiral casing, stay vanes, guide vanes (GVs), and the runner, defined as h_{01}.

$$h_{01} = E_0 - E_1 - H_R \tag{2.10}$$

Rewriting Equation 2.2 with Equation 2.8, Equation 2.9 and Equation 2.10, we get that the head is the sum of useful head and losses, $h = h_{01} + h_{DT} + h_{out}$.

$$H = H_R + h \tag{2.11}$$

Finally, Equation 2.1 can be rewritten as a function of the losses associated with the draft tube; h_{DT} and h_{out}.

$$\eta_h = \frac{H_R}{H_R + h} = \frac{H_R}{H_R + h_{01} + h_{DT} + h_{out}} \tag{2.12}$$

Equation 2.12 shows that DT losses are inversely related to hydraulic efficiency. Thus improve the DT performance increases the efficiency of the hydropower plant.

2.1.3 Performance characteristics

The most common characteristic used in draft tube optimization is the pressure recovery factor, C_p. It reflects the increase of pressure head throughout the DT.

$$C_p = \frac{\frac{1}{Q}\iint_{A_2}(\frac{p}{\rho g} + z)(\boldsymbol{c} \cdot d\boldsymbol{A}) - \frac{1}{Q}\iint_{A_1}(\frac{p}{\rho g} + z)(\boldsymbol{c} \cdot d\boldsymbol{A})}{E_{k,Q,1}} \tag{2.13}$$

Index 1 and 2 denote the inlet and the outlet of the DT and $E_{k,Q,1}$ is defined by Equation 2.7. High C_p is desirable as it indicates that the DT can reduce the pressure of the runner outlet effectively. Rewriting Equation 2.13 with the theory presented in subsection 2.1.2, C_p can also be expressed as:

$$C_p = \frac{E_{k,1}}{E_{k,Q,1}} - \left(\frac{A_1}{A_2}\right)^2 - \frac{(h_{DT} - h_{out})}{E_{k,Q,1}} \tag{2.14}$$

Assuming an ideal DT with no losses, the ideal pressure recovery factor will simplify to $C_{p,ideal} = \frac{E_{k,1}}{E_{k,Q,1}} - \left(\frac{A_1}{A_2}\right)^2$. Hence, the efficiency of the DT in terms of pressure recovery, is defined as:

$$\eta_{C_p} = \frac{C_p}{C_{p,ideal}} \tag{2.15}$$

The DT efficiency would improve by reducing the losses. Thus, the DT performance can be discussed in terms of the energy loss coefficient, ξ.

$$\xi = \frac{h_{DT}}{E_{k,Q,1}} \tag{2.16}$$

A low ξ is desirable, whereas h_{DT} defines the hydrodynamic losses in the DT.

2.1.4 Draft tube topology

A curved DT consists of three major parts, the cone, the elbow, and the exit diffuser. The water first enters the cone from the outlet of the runner. It then flows through the elbow, the curved part, and is discharged through the exit diffuser. The direction tangential to the center axis of the DT is referred to as the meridional direction. The DT topology is illustrated in Figure 2.3.

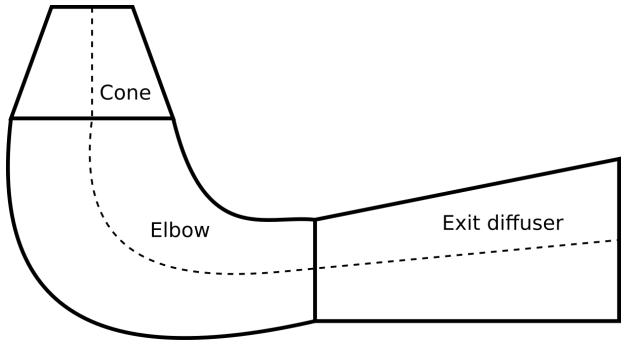

Figure 2.3: Curved DT topology, showing the three main parts: the cone, the elbow ,and the exit diffuser. The dashed line illustrates the DTs symmetry axis. The flow direction tangential to this axis is defined as the meridian direction.

2.1.5 Flow phenomenon

The flow in the DT is complex due to unsteadiness, turbulence, separation, curvature and secondary flow, swirl, and vortex breakdown [5]. The flow is also highly dependent on the OP of the turbine.

Turbulence

Turbulence is described as fluctuations in the flow field. It is complicated as it is three dimensional in space, unsteady, and consists of many time and length scales. A flow becomes turbulent when the inertia forces dominate over the viscous forces, which is related to a high Reynolds number (Re). Internal flow is defined as turbulent when Re exceeds 4000.

Swirling flow

The velocity triangles in Figure 2.4 illustrate how the flow enters the DT at various OPs. The velocity triangles display the relationship between the velocity of the water, the runner speed, u, and the velocity of the water relative to the runner blade w. The vectors will always form a triangle based on the relation $\vec{w} = \vec{c} - \vec{u}$ and the direction of $\vec{w}$ will always be approximately tangential to the blade curvature at the runner outlet.

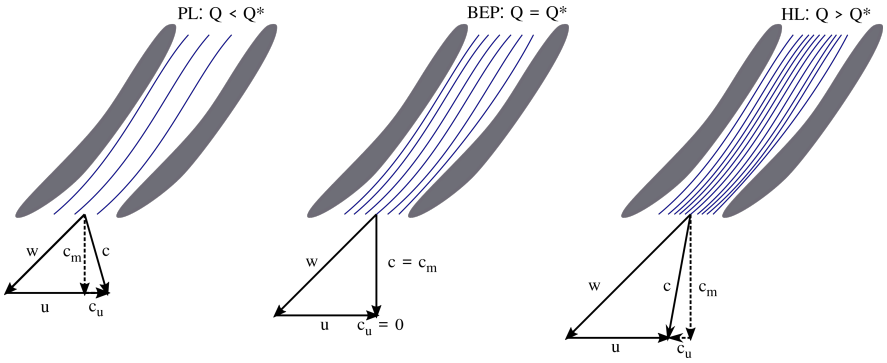

Figure 2.4: Runner outlet velocity triangles for PL, BEP and HL operation. c_m and c_u is the axial and tangential velocity component of the water, while w is the velocity of the water relative the runner blade with speed u, and Q is the discharge.

The tangential velocity of the water leaving the runner is associated with losses. Hence when a Francis turbine is operating at BEP, the water enters the DT in approximately the axial direction, meaning $c \approx c_m$.

When operating at PL, $Q < Q^*$ and the axial velocity of the water c_m is reduced. A swirling component, c_u, in the rotating direction of the runner is introduced to maintain the fixed relation between w and u. In contrast, operating at HL, $Q > Q^*$ and the axial velocity of the water is increased. This imposes a tangential component of the water in the opposite direction.

Vortex breakdown and backflow

When the discharge is reduced from operating with approximately axial flow to operating with increased tangential velocities, a sudden change in the flow regime will occur if the swirl becomes strong enough. This phenomenon is called a vortex breakdown, and the concept is analogous with hydraulic jumps in open-channel flows [16]. The swirling flow entering the DT separates into two concentric regions:

an outer region where the primary fluid transport occurs and an inner region which may contain a stagnation zone or a dead water core. A pressure gradient outwards in the radial direction from the DT center axis occurs, creating a low-pressure region in the middle part of the cone. Secondary flow along the DTs center axis may be present as a consequence of the unfavorable pressure gradient. The phenomenon is called backflow and illustrated in Figure 2.5. Vortex breakdown gives rise to a rotating vortex rope around the DT center axis. Its shape is a helical corkscrew, and it is a highly transient flow phenomenon. The rotating vortex rope becomes visible if cavitation is present, due to a low-pressure region in its center.

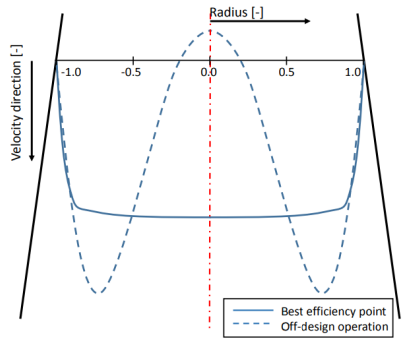

Figure 2.5: Theoretical axial velocity profiles in a DT [1].

Cavitation

If the static pressure of the water drops below the vapor pressure, cavitation will occur. Small cavities of vapor will form and move into higher pressure regions where they collapse and implode. This blocks the flow and reduces the DT performance. The local pressure and temperature at the cavity center increase tremendously, which may damage the surrounding material. The risk of cavitation increases when operating at off-design conditions, and the higher the turbine is placed above the tailwater.

Cavitation column

If the swirl becomes high enough when operating at HL, a standing cavitation column located symmetrically around the DT centerline will occur. If the frequency of the cavitation column is near resonance with the standing wave frequency of the DT, the cavitation column is pulsating, which leads to mass flow oscillations in the entire hydropower plant.

Surge

Vortex breakdown, cavitation, the rotating vortex rope, and the cavitation column lead to pressure fluctuations in the DT, denoted the surge. The pressure fluctuations propagate to other parts of the hydropower plant, which leads to unstable power production.

Wall separation

If the cross-section area of the DT diverges too much, boundary layer separation will occur. This leads to recirculating zones close to the walls, which block the flow and give rise to pressure losses. The radial pressure gradient from a swirling flow decreases the possible flow separation. Thus, reaction turbines are often designed to have a small swirling component of the water entering the DT [17].

Flow in curved conduits

The DT elbow forces the fluid to change direction to a curvature pathway. This leads to increased pressure at the outer wall and decreased pressure at the inner wall of the bend. The velocity will decrease on the pressure side and increase at the suction side. After the bend, the flow close to the inner wall slows down. The flow close to the outer wall accelerates. This variation in flow velocity can cause separation and eddy zones at both the inner and at the outer wall.

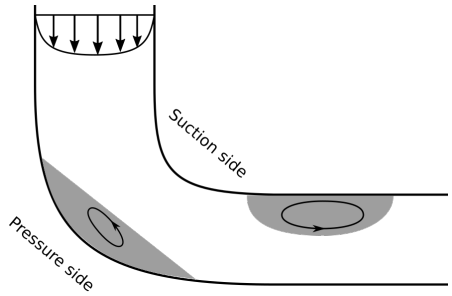

Figure 2.6: Possible separation and eddy zones in a pipe bend.

The phenomenon of separation downstream of the elbow can be reduced by contracting the draft tubes cross-section area slightly in the elbow [2]. The convergent section helps the flow to follow the wall curvature and by this reduce hydraulic losses. The cross-sectional area along a contracting elbow is illustrated in Figure 2.7.

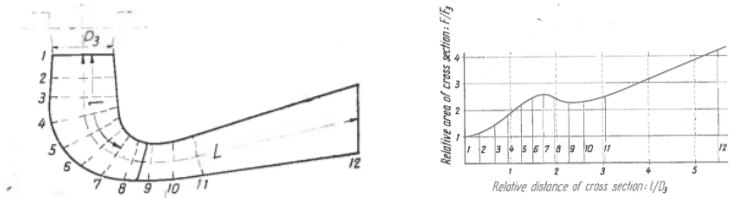

(a) Cross-section locations **(b)** Relative area of cross sections

Figure 2.7: Suggested relationship between cross-sectional area locations (a) and relative areas (b) for a DT with a contracting elbow [2].

2.2 Modeling theory

The software ANSYS is utilized for CFD calculations in the following research. It is an element-based finite volume method, which implies that the spatial domain is discretized into finite volumes. Quantities such as mass and momentum are conserved for these volumes during the simulation. The most relevant modeling theory for the following work is presented in this section. It is primarily written with the ANSYS 2020R1 User guides [3, 18–20] as references.

2.2.1 Types of errors

CFD calculations strive to predict the physical behavior of flows. However, the results will always include uncertainties due to various sources of errors. Modeling errors represent the most significant factor of uncertainty. They are results of the necessity to describe flow aspects such as turbulence by an empirical turbulence model or assuming transient effects to be irrelevant. Discretization errors represent the difference between the solution provided by the exact equations and the discretized ones solved by the CFD code. The quality of the mesh utilized and the choice of discretization schemes are the significant sources of numerical error.

Additionally, iteration error related to a not fully converged solution and round-off errors related to the numerical decimal precision of the computer also contributes to the numerical uncertainty. The overall precision of CFD calculations may also be affected by user errors, application uncertainty, and software errors. User errors are caused by incorrect use of the CFD software, as application uncertainty is related to insufficient information to define a simulation. Last mentioned can, by example, be insufficient information to describe a boundary condition. Software error denotes inconsistently between documented equations and the actual implementation in the CFD software.

Accuracy of a CFD prediction is checked by verification, validation, and numerical accuracy tests. Verification is the process of ensuring that the programming and computational implementation is correct. As Ansys is a closed source software, no source code is available. However, Ansys is extensively used for research and in the industry, and is ranked among the best CFD software available [21]. Validation involves comparing CFD results to experimental data. Numerical accuracy can be indicated by the Grid Convergence Index(GCI). This method is further described in subsection 2.2.8.

2.2.2 Turbulence modeling

The small length scales of turbulent flow require an extremely fine discretization to resolve the general Navier Stokes equations for mass and momentum conservation

correctly. Such fine mesh does not apply to numerical analysis and would require enormous computational power. To enable the effects of turbulence to be predicted, a wide range of turbulence models have been developed.

The k-ϵ model

The k-ϵ turbulence model is chosen for the work. It is an eddy viscosity turbulence model, which models turbulence as small eddies that are continuously forming and dissipating. The $k-\epsilon$ model introduces two variables, namely the turbulent kinetic energy k, and the turbulence eddy dissipation ϵ. k defines the variance of the fluctuations in velocity as ϵ defines the rate in which the velocity fluctuations dissipate.

The $k-\epsilon$ model offers comprise in terms of accuracy and robustness. However, it shows weakness when predicting flows with boundary layer separation, rotating fluids, and flows over curved surfaces. The presence of swirling flow can lead to an over-prediction of turbulent mixing and decay of the core vortex. Although all these flows are present in a DT, several optimization studies are utilizing the $k-\epsilon$ model [15, 22, 23]. There exist curvature correction models in ANSYS' $k-\epsilon$ model, but they have not been generally validated for complex flows. Notably, choosing $k-\epsilon$ as the turbulence model will lead to modeling errors. However, the objectives of interest in the research are calculated from averaged quantities of pressure and velocities, so the modeling errors from turbulent uncertainties might not be considerable.

2.2.3 Govern equations

Eddy viscosity turbulence models are statistical models that assume that flow quantities can be decomposed into one mean- and one fluctuating part. This is substituted into the Navier-Stokes equations, which are further time-averaged. The resulting modification is called the Reynolds Averaged Navier-Stokes (RANS) equations. They describe time-averaged conservation of mass and momentum and are defined by ANSYS CFX as:

$$\frac{\partial \rho}{\partial t} + \frac{\partial}{\partial x_j}(\rho c_j) = 0 \tag{2.17}$$

$$\frac{\partial \rho c_i}{\partial t} + \frac{\partial}{\partial x_j}\left(\rho c_i c_j\right) = -\frac{\partial p'}{\partial x_i} + \frac{\partial}{\partial x_j}\left[\mu_{eff}\left(\frac{\partial c_i}{\partial x_j} + \frac{\partial c_j}{\partial x_i}\right)\right] + S_M \tag{2.18}$$

The left side of Equation 2.18 represents inertia forces, and the right-hand side is

a sum of pressure forces, viscous forces, and external forces. p' is the modified pressure defined as:

$$p' = p + \frac{2}{3}\rho k \tag{2.19}$$

μ_{eff} is the effective viscosity, defined as the sum of the dynamic viscosity μ and turbulent viscosity μ_t. The eddy viscosity model introduces the turbulent viscosity due to additional turbulent stresses. For the $k-\epsilon$ model, it is defined as:

$$\mu_t = \rho C_\mu \frac{k^2}{\epsilon} \tag{2.20}$$

Where C_μ is an empirical constant. The k-ϵ model is a two-equation model as it introduces two additional transport equations of the turbulent kinetic energy and the dissipation rate:

$$\frac{\partial(\rho k)}{\partial t} + \frac{\partial}{\partial x_j}(\rho c_j k) = \frac{\partial}{\partial x_j}\left[\left(\mu + \frac{\mu_t}{\sigma_k}\right)\frac{\partial k}{\partial x_j}\right] + P_k - \rho\epsilon \tag{2.21}$$

$$\frac{\partial(\rho \epsilon)}{\partial t} + \frac{\partial}{\partial x_j}(\rho c_j \epsilon) = \frac{\partial}{\partial x_j}\left[\left(\mu + \frac{\mu_t}{\sigma_\epsilon}\right)\frac{\partial \epsilon}{\partial x_j}\right] + \frac{\epsilon}{k}\big(C_{\epsilon 1} P_k - C_{\epsilon 2}\rho\epsilon\big) \tag{2.22}$$

$C_{\epsilon 1}$, $C_{\epsilon 2}$, σ_k, σ_ϵ are empirical constants and P_k is the turbulence production due to viscous forces. An overview of the values of the empirical constants and further definition of the turbulence production term is presented in Appendix A.

2.2.4 Mesh

The mesh is a discrete representation of the geometric domain. It consists of small sub-domains called elements. The simulation time and the numerical error is highly dependent on the number of nodes and elements, and the elements shape and dimensions. In general, a high number of elements gives more accurate results, but also increases the computational time. On the other hand, having too few elements can lead to a miscalculated response or convergence failure. The elements can take different shapes, as illustrated in Figure 2.8.

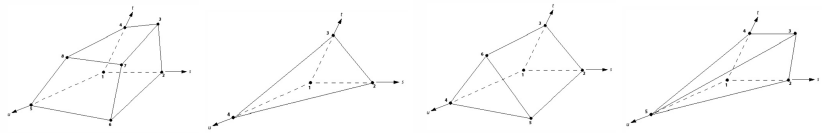

(a) Hexahedral **(b)** Tetrahedral **(c)** Wedge **(d)** Pyramid

Figure 2.8: Different shape configurations of mesh elements [3].

Calculations of normal vectors and fluxes typically have less round of errors for hexahedral elements, compared to tetrahedral, wedge and pyramid elements. A structural mesh consists of hexahedral elements, whereas an unstructured mesh can be comprised of all types of elements. The storage of a structural mesh is more efficient in the computer memory. Thus, a simulation of a structural mesh will use less computational time than an unstructured mesh. The advantage of an unstructured mesh is that it is easier to build if the geometry is very intricate.

The ANSYS CFX 2020R1 Reference Guide [18] lists several guidelines for how to perform a successful mesh generation:

- Avoid high mesh stretching ratios.
- Avoid jumps in mesh density.
- Avoid poor mesh angles.
- Avoid non-scalable mesh topologies.
- Avoid non-orthogonal elements in boundary layers.
- Use a finer grid in more critical areas.

The overall quality of a mesh can be checked against various mesh metric variables. ANSYS CFX post evaluates the mesh in terms of orthogonality, volume expansion, and aspect ratio. Orthogonality relates to how close the angles between adjacent element faces or adjacent element edges are to some optimal angle, e.g., 90° for a squared surface. Poor orthogonality angels are a source of discretization error and difficulties with obtaining a converged solution. Volume expansion relates to the rate of change in the magnitude of adjacent volumes. High volume expansion ratios may lead to discretization errors of transient and body force terms. Aspect ratio is a measure of how much an element is stretched. If an element is too stretch, the consequence may be round-off errors and difficulties with obtaining a converged

solution. Element Quality, Aspect Ratio, Jacobian Ratio, Warping Factor, Parallel Deviation, Maximum Corner Angle, Skewness, Orthogonal Quality, and Characteristic Length are additional mesh metric variables provided by ANSYS Meshing. A more detailed explanation of each variable is found in Ansys Meshing User Guide [20].

2.2.5 Discretization schemes

The mesh is utilized for building control volumes. The CFX-solver is vertex-oriented, which means that the control volumes are centered around the vertices of the elements. The solution variables and fluid properties are stored in the nodes located at the vertices. Cell-centered is another control volume orientation, and the difference between the two approaches is illustrated in Figure 2.9.

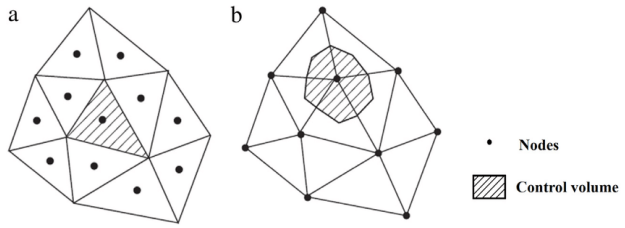

Figure 2.9: Cell-centered (a) and a vertex-centered (b) control volumes illustrated on triangular 2D mesh elements [4].

The governing equations are solved for each control volume by integrating the terms of the partial derivatives into either volume or surface integrals. The volume and surface integrals are further approximated with discretization schemes, which are solved during a simulation.

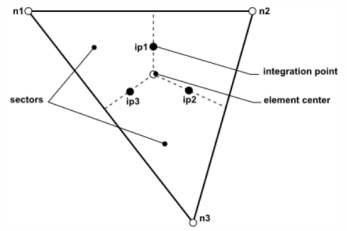

Figure 2.10: Illustration of volume sectors and integration points within a mesh element [3].

Figure 2.10 illustrates how a mesh element is divided into sectors. Lines divide the element from the center of the edges to the center of the element. Integration points are located at the center of these lines. In general, volume integrals are discretized within each element sector and further accumulated to the sector's control volume. Surface integrals are discretized at the integration points and then distributed to the adjacent control volumes.

The numerical error associated with the schemes is related to the order of the scheme of accuracy. It is found, by a series expansion of the schemes truncated part, and can be measured in terms of both spatial lengths or time step. A high order of accuracy generally implies that errors are reduced more quickly with mesh or time step size refinement. This comes with the disadvantages of increased computational load and typically less robustness. ANSYS CFX uses second-order accurate approximations as much as possible. A detailed description of all terms of the governing equations is given in the Ansys CFX 2020R1 Solver Theory Guide [3]. The choice of discretization scheme for the advection term must be chosen prior a simulation. For transient simulation, a time discretization scheme must also be chosen.

Advection schemes

In general, Ansys CFX defines the advection scheme for an arbitrary variable ϕ as:

$$\phi_{ip} = \phi_{up} + \beta \nabla \phi \cdot \Delta \vec{r} \tag{2.23}$$

Where ϕ_{ip} is the value of the variable in an integration point, ϕ_{up} is the variable value in the upwind node, and $\vec{r}$ is the vector from the upwind node to the integration point. β and $\nabla \phi$ denotes a blending factor and the advective flux. The different advection schemes are dependent on the choice of β and $\nabla \phi$.

$\beta = 0$ corresponds to the first order Upwind Difference Scheme. It is very robust, but the low order of accuracy introduces an artificial diffusion term. This smears out gradients in the solution, making the numerical error large.

Specified Blend Factor is another option, where β can be specified, and the order of accuracy increases with β. This may reduce the artificial diffusion, but might introduce dispersive discretization errors. Dispersive discretization errors are seen as artificial oscillations in regions of steep gradients and is a result of an unbounded scheme.

The Central Difference Scheme is second-order accurate as $\beta = 1$, and ϕ evaluated in the local element. This scheme might also lead to dispersive errors and is not recommended with models other than the LES turbulence model.

The High Resolution scheme strikes a good balance between robustness and accuracy. β is calculated locally for each node. It is chosen to be as close to 1 as possible without introducing dispersion with new extremes. This way, the order of the accuracy of the scheme is as close to second-order as possible. The advective flux is evaluated in the upwind node.

2.2.6 Modeling flow near the wall

Turbulent flow close to a wall is characterized by steep velocity gradients and the presence of large viscous effects. To fully solve the turbulent boundary layer, an extremely fine mesh close to the wall is required. Such fine meshes are built with thin inflation layers, which results in a high number of elements and high computational time. An alternative is to model the flow close to the wall with a wall function. Thus a coarser mesh can be utilized and computational resources saved.

Experiments and mathematical analysis show that the turbulent boundary layers can be divided into different regions. Closest to the wall is the viscous sublayer, where molecular viscosity dominates the momentum transport, and the flow is approximately laminar. Further out is the logarithmic layer, where turbulence dominants the mixing process. Between these two layers is the buffer layer, where both the effect of molecular viscosity and turbulence are of equal importance.

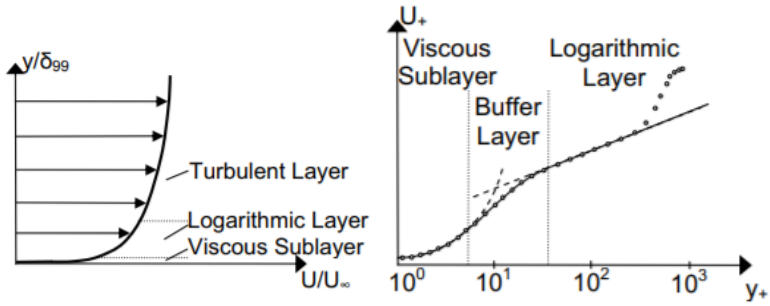

(a) Linear plot **(b)** Log-linear plot

Figure 2.11: Mean velocity profiles in turbulent boundary layers [5].

Figure 2.11(a) shows an overview of the different regions in a turbulent boundary layer as Figure 2.11(b) shows a close up of the inner region where y^+ and u^+ are scales of the distance from the wall and the tangential velocity. Boundary layer theory shows that the relationship can be approximated as linear, $u^+ = y^+$, in

the viscous sublayer. In the logarithmic sublayer, the relationship is shown to be logarithmic. This concept is famously known as the *log law of the wall*, which gives rise to the wall function defined as:

$$u^+ = \frac{u}{u_\tau} = \frac{1}{\kappa} ln(y^+) + C \tag{2.24}$$

Where κ is the von Karman constant and C is the log-layer constant depending on the wall roughness. Further is y^+ defined as:

$$y^+ = \frac{y u_\tau}{\nu} \qquad u_\tau = \left(\frac{\tau_w}{\rho}\right)^{1/2} \tag{2.25}$$

Where y is the distance from the wall, ν is the kinematic viscosity, u_τ is the friction velocity, τ_w is the wall shear stress, and ρ is the density. Equation 2.25 defines the y^+ value for the node closest to the wall by letting $y = \Delta y$ be the distance from the wall to the first node. The velocity of the first node is then calculated from Equation 2.24. When using a wall function, it is essential that the y^+ value of the first node is placed within the logarithmic region. Additionally, it is recommended to place at least 10 nodes within the turbulent boundary layer to resolve it entirely.

The range of the logarithmic regions depends on the flow. A widely used correlation assumes the lower limit of the logarithmic layer to be $y^+ \geq 30$ and the upper limit to be $\frac{y}{\delta} < 0.2$, where δ is the length of the turbulent boundary layer [24]. Defining the turbulent Reynolds number as $Re_\tau = \frac{\delta u_\tau}{\nu}$, the range of y^+ in the logarithmic region of the turbulent BL is given by:

$$30 \leq y^+ \leq 0.2 \cdot Re_\tau \tag{2.26}$$

A comparison between the wall function and experimental data is presented in Figure 2.12. The upper limit of the logarithmic region denotes where the logarithmic wall function stops correlating with the experimental data. The upper limits are seen to vary dependent on the Reynolds number of the flow. However, an upper limit of the logarithmic region of about $y^+ \sim 200 - 300$ can be observed as a sufficient minimum limit of the represented flows.

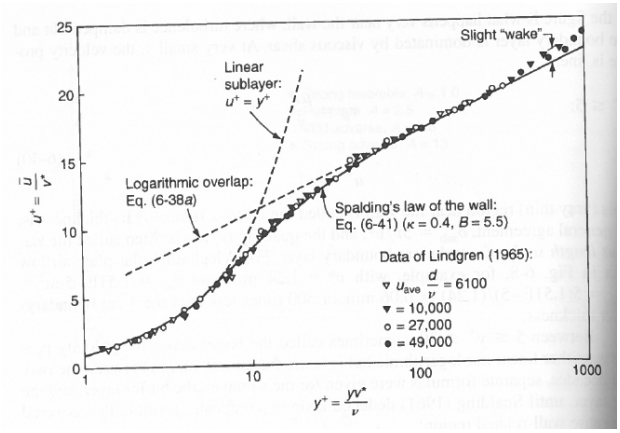

Figure 2.12: Wall function compared to experimental data for different Reynolds numbers [6].

The $k - \epsilon$ turbulence model in Ansys CFX uses a scalable wall function. In simple terms, this involves that y^+ in the first node is never taken to be lower than 11.06. This is because the logarithmic law is assumed to model the flow in the buffer layer better than the linear assumption for $y^+ \geq 11.06$. As a result, the $k - \epsilon$ model will work, even when the mesh is too fine. However, it is not preferable to have such fine mesh as it would be computationally expensive and give an inaccurate picture of the flow field.

2.2.7 Convergence

The sets of algebraic equations solved in a simulation are related by non-linearity and require an iterative approach to be solved. It is essential to achieve a satisfactory converged result with a low iterative error. For each iteration, a residual is reported as a measure of the error related to the overall conservation of the flow properties. A converged result is characterized by a reduction in the residuals. Convergence can also be observed by keeping track of the flow variables at fixed locations with monitor points. When the flow variables are stabilizing at approximately fixed values, convergence is indicated.

The convergence rate can be controlled by changing the time step. It works as an "acceleration parameter" by reducing the number of iterations required to reach convergence for a steady-state simulation, or the number of iterations required for each time step in a time-dependent analysis. For steady-state modeling, a false time step is applied by the CFX solver, which normally under-relaxes the equations as

they iterate towards the final solution. However, the equations solved are implicit, so by increasing the time scale, a converged solution can usually be found faster. On the other hand, if the time scale used is too large, the resulting convergence behavior will become fluctuating. The time step can be controlled in several ways by changing the time scale factor. This scales the time step calculated by the CFX solver. A more detailed description of how the solver calculates the time scale is found in the ANSYS CFX 2020R1 Solver Theory guide [3].

2.2.8 Grid independent solution

A grid-independent solution means that the result of a CFD simulation does not change when the mesh is refined. It is desirable to decrease the discretization error. The Grid Convergence Index (GCI) measures the percentage a computed value is away from the asymptotic numerical value. In other words, a low GCI value indicates that the simulation results are close to being grid-independent.

The GCI-Method by Celik [25] can be performed to calculate the GCI-value of a mesh. The method is based on the central philosophy of comparing the results of simulations done with three different mesh resolutions. The final GCI-value is defined as:

$$GCI = \frac{1.25 e_a}{r^p - 1} \tag{2.27}$$

e_a is the approximate relative error between two simulations, r is a refinement factor between grids, and p is the apparent order of the method. A more detailed explanation of how the GCI-Method is performed is attached in Appendix B.

2.2.9 Modeling flows in rotating domains

Modeling flow in a rotating frame is done by applying external forces, $\boldsymbol{S}_{M,rot}$, to the govern equation defined in Equation 2.18.

$$\boldsymbol{S}_{M,rot} = \boldsymbol{S}_{cor} + \boldsymbol{S}_{cfg} \tag{2.28}$$

The rotational forces is a sum of Coriolis forces, $\boldsymbol{S}_{cor}$, and centrifugal forces, $\boldsymbol{S}_{cfg}$, defined as:

$$\boldsymbol{S}_{cor} = -2\rho\omega \times \boldsymbol{U} \tag{2.29}$$

$$\boldsymbol{S}_{cfg} = -\rho\omega \times (\omega \times \boldsymbol{r}) \tag{2.30}$$

ω is the angular velocity of the rotational domain, $\boldsymbol{r}$ is the distance from the rotational axis, and $\boldsymbol{U}$ is the velocity in the rotating frame of reference.

In the present study, the runner is simulated together with the stationary domains of the GVs and the DT. This requires further domain interface models, further described in subsection 2.2.10.

2.2.10 Domain interface modeling

Domain interface models are methods for connecting or matching meshes. Ansys CFX offers three different options: Translational periodicity, rotational periodicity, and general connection.

Rotational periodicity is an option for simplifying repeating, periodic interfaces. The mesh of passages around guide vane blades or runner blades can be simplified to only contain one passage, by connecting the two faces in the peripheral direction. By this, the method assumes a symmetric axis flow, which could be a source of modeling errors. The benefit of the method is a reduced domain, which reduces the computational cost.

General connection is an option used when meshes with a different frame of reference and/or meshes of different sizes are connected. The option got the three models: Frozen rotor, stage, and transient rotor-stator, for modeling the change in frame of reference.

Frozen rotor is a steady-state approach where the flow is modeled from one domain to the next, by assuming the relative position of the domains to be fixed. In other words, it tries to find a steady-state solution for a "frozen rotor". The fluxes are mapped from one interface to the other and scaled by the eventual pitch difference. However, the modeling errors can be considerable since it neglects transient effects on the interface and fixes the runner for a particular position.

Stage (mixing-plane) model is also a steady-state model, which performs a circumferential averaging of the fluxes on the interfaces. This accounts for time average effects between the blade passages but neglects transient effects at the surfaces as.

The transient rotor-stator model is the last frame change/mixing model, which are modeling transient behavior. This is the most realistic model, but also the most computationally expensive.

2.3 Optimization theory

Design optimization may be performed several ways. Cavazutti presents an overview of theory and different techniques related to the theme [26]. This thesis is performed with Surrogate-based Optimization (SBO).

2.3.1 Surrogate-based optimization

This section is written with Marjavaaras doctoral thesis about CFD driven SBO as a reference [5].

The steps of an SBO analysis are summarized in Figure 2.13. The strategy is to build mathematical functions, namely surrogate models, which are used to discuss optimal designs. Surrogate models approximate performance characteristics of interest. The performance characteristics are called objectives, and their corresponding surrogate models is commonly called the objective functions.

Figure 2.13: Flow chart of the steps of a Surrogate-based optimization analysis.

1. Geometric Parameterization

The first step is to create a parametric design of the geometry with N design variable (DVs). The DT geometry will also depend on some design constraints, i.e., a linear change of one DV to another or curvature controlled by Bezier curves. However, the design constraints describe fixed relations between the DVs for the entire optimization, in contrast to the DVs, which vary. Further, must a lower, x_i^l, and an upper, x_i^u, limit for each design parameter, x_i be specified. The range of all the design parameters is called the design space (DS).

$$\text{Design variables: } \boldsymbol{x} = (x_1, x_2, ..., x_N) \tag{2.31}$$

$$\text{Design space: } x_i^l \leq x_i \leq x_i^u \quad , \quad i = 1, 2, ..., N \tag{2.32}$$

2. Design of Experiment

Secondly, the design space is populated in M samples, which are called design points (DPs), by using a Design of Experiments (DOE) method.

$$\text{Design points:} \quad \boldsymbol{x}^{(1)}, \boldsymbol{x}^{(2)}, ..., \boldsymbol{x}^{(M)} \quad , \quad \boldsymbol{x}^{(j)} = x_1^{(j)}, x_2^{(j)}, ..., x_N^{(j)} \tag{2.33}$$

DOE is used for guiding the choice of the experiments to be performed in an efficient way [26]. The goal is to obtain the required information with a minimum of sampling points. Box-Behnken Design (BBD) and Full Factorial Designs are examples of DOEs.

3. Computer Analysis

The samples are investigated in step 3 by CFD calculation. The objective(s) of interest are obtained from simulations of each DP.

$$\text{Objective data:} \quad y^{(1)}, y^{(2)}, ..., y^{(M)} \tag{2.34}$$

4. Surrogate Model Construction

The data is used to build objective functions in step 4. The goal is to find a function, $\hat{y}(\boldsymbol{x})$, which fits simulation results such that:

$$\hat{y}(\boldsymbol{x}^{(1)}) \approx y^{(1)}, \hat{y}(\boldsymbol{x}^{(2)}) \approx y^{(2)}, ..., \hat{y}(\boldsymbol{x}^{(M)}) \approx y^{(M)} \tag{2.35}$$

Response surface modeling (RSM) is a commonly used surrogate modeling technique that fits the simulated results as second-order polynomials.

5. Result discussion

Optimal designs are discussed in step 5 by utilizing the objective function(s). The object function predicts the objective performance of numerous designs much faster than CFD simulations. Thus large numbers of designs can be explored. If an optimization problem involves several objectives, the problem is called a multi-objective optimization problem. Thus an optimal design is discussed as a trade-off in improvements in the objectives.

2.3.2 Bézier curves

Bézier curves are parametric curves commonly used in computer graphics [27]. They are built up by Bernstein polynomials, $b_{i,n}(t)$, defined as:

$$b_{i,n}(t) = \binom{n}{i} t^i (1-t)^{n-1} \quad , \quad i = 0, 1, ..., n \tag{2.36}$$

$n \in \mathbb{N}$ defines the degree of the curve, and $t \in [0, 1]$ is the parameter of the curve. The French engineer Pierre Bézier developed the Bézier curves in 1960. The curve is controlled by $n+1$ control points $\boldsymbol{P}_i$, which define a control polygon. Mathematically, an n[th] order Bézier curve is given as:

$$\boldsymbol{B}(t) = \sum_{i=0}^{n} b_{i,n}(t)\boldsymbol{P}_i \quad , \quad 0 \leq t \leq 1 \tag{2.37}$$

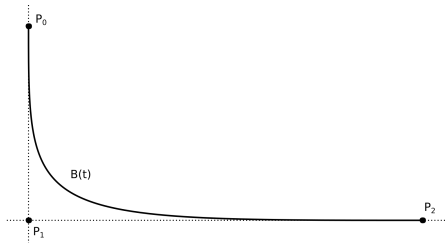

Figure 2.14: Illustration of a quadratic Bézier curve.

A second-order Bézier curve, also known as a quadratic Bézier curve is illustrated in Figure 2.14. From Equation 2.36 and Equation 2.37, the parametric description of the curve becomes:

$$\boldsymbol{B}(t) = (1-t)^2\boldsymbol{P}_0 + 2t(1-t)\boldsymbol{P}_1 + t^2\boldsymbol{P}_2 \quad , \quad 0 \leq t \leq 1 \tag{2.38}$$

$\boldsymbol{P}_0$ denotes the starting point, and $\boldsymbol{P}_2$ denotes the ending point. The nature of a Bézier curve makes the derivative in the starting point parallel to the tangent between $\boldsymbol{P}_0$ and $\boldsymbol{P}_1$. Similarly, the slope at the ending point is parallel to the tangent between $\boldsymbol{P}_1$ and $\boldsymbol{P}_2$. Thus, $\boldsymbol{P}_1$ can be utilized to control curvature. The derivative of the quadratic Bézier curve is defined as:

$$\boldsymbol{B}'(t) = 2(1-t)(\boldsymbol{P}_1 - \boldsymbol{P}_0) + 2t(\boldsymbol{P}_2 - \boldsymbol{P}_1) \quad , \quad 0 \leq t \leq 1 \tag{2.39}$$

2.3.3 Box-Behnken Design

BBD was created by George E. P. Box and Donald Behnken in 1960 to be a DOE method that supported RSM [28].

BBD is an DOE method based on incomplete three-levels full factorial design [26]. The term *level* indicates that each variable takes three different values - a lower, a central, and an upper value. Full factorial design is another DOE method that includes all possible combinations of the DVs for a given level. By this, the three-levels full factorial design gives a total of $m = 3^n$ samples, where n is the number of DVs.

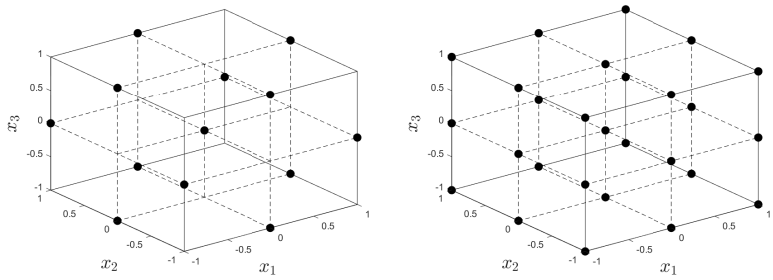

(a) Box-Behnken Design **(b)** Three level Full Factorial Design

Figure 2.15: A sampling comparison between Box-Behnken Design(a) and Three Level Full Factorial Design (b) for $n = 3$ design variables. The black dots are design points of the sample, and the values -1, 0 and 1 correspond to the lower-, center- and upper value of the the design variables. The solid lines represents the limit of the design space and the vertices corresponds to extremes.

BBD is built up by blocks of DPs that consist of some DVs combined like a Full Factorial Design, and some DVs kept constant at their center values.

The DPs are combined in a particular manner to facilitate rotatability. A rotatable design means that the variance of the predicted response at any point is a function of the distance from the center value alone. The center point, meaning the DP where all DVs equals their center value, is usually added some extra times to the sampling, to reduce the variance.

Compared to three-level Full Factorial Design, BBD limits the order of samples for higher numbers of parameters. This reduces the computational time needed. BBD also avoids extremes, meaning samples where all the design variables equal their upper or lower limits. Hence, numerical uncertainty might be reduced as extreme designs typically can have problems converge [29]. However, avoiding extreme designs leads to more significant uncertainty in such part of the design space. This restricts the center values to be chosen close to the optimal design to obtain an accurate prediction.

2.3.4 Response surface modeling

This section is written with Myers' book: Response Surface Methodology [30] as a reference.

RSM fits data into a polynomial predictor, denoted by $\hat{y}(\boldsymbol{x})$. The predictor is a function of n DVs, $\boldsymbol{x} = x_1, x_2, ..., x_n$, and a second order RSM is defined as:

$$\hat{y}(\boldsymbol{x}) = \beta_0 + \sum_{i=1}^{n} \beta_i x_i + \sum_{i=1}^{n-1} \sum_{j>i}^{n} \beta_{ij} x_i x_j + \sum_{i=1}^{n} \beta_{ii} x_i^2 \tag{2.40}$$

x_i corresponds to linear terms, x_i^2 - quadratic terms, $x_i x_j$ - interaction terms, and β are unknown regression coefficients. The minimum number of data samples needed to estimate β are $p = (n+1)(n+2)/2$. The difference between the RSM approximation and the real objective value, $y(\boldsymbol{x})$, is represented with a random error ϵ.

$$y(\boldsymbol{x}) = \hat{y}(\boldsymbol{x}) + \epsilon \tag{2.41}$$

BBD always define m samples so that $m \geq p$ and the problem is overdetermined. Further more, the fitting problem is solved by Least Square Minimization of the error. In matrix notation, Equation 2.41 can be written as:

$$\boldsymbol{y} = \boldsymbol{X}\boldsymbol{\beta} + \boldsymbol{\epsilon} \tag{2.42}$$

$\boldsymbol{y} = y^{(1)}, y^{(2)}, ..., y^{(m)}$ are the sample targets collected, $\boldsymbol{X}$ is a $m \times p$ matrix of the linear, quadratic and mixed DVs terms, and $\boldsymbol{\beta}$ and $\boldsymbol{\epsilon}$ are column vectors of size $p \times 1$ and $m \times 1$.

$$\boldsymbol{X} = \begin{bmatrix} 1 & x_1^{(1)} & \cdots & x_n^{(1)} & x_1^{(1)}x_2^{(1)} & \cdots & x_{n-1}^{(1)}x_n^{(1)} & \left(x_1^{(1)}\right)^2 & \cdots & \left(x_n^{(1)}\right)^2 \\ \vdots & \vdots & \ddots & \vdots & \vdots & \ddots & \vdots & \vdots & \ddots & \vdots \\ 1 & x_1^{(m)} & \cdots & x_n^{(m)} & x_1^{(m)}x_2^{(m)} & \cdots & x_{n-1}^{(m)}x_n^{(m)} & \left(x_1^{(m)}\right)^2 & \cdots & \left(x_n^{(m)}\right)^2 \end{bmatrix} \tag{2.43}$$

The square of the error can further be defined as:

$$L = \sum_{i=1}^{n} \epsilon_i^2 = \boldsymbol{\epsilon}^T \boldsymbol{\epsilon} = (\boldsymbol{y} - \boldsymbol{X}\boldsymbol{\beta})^T (\boldsymbol{y} - \boldsymbol{X}\boldsymbol{\beta}) \tag{2.44}$$

Least Square Minimization estimates the regression coefficients $\boldsymbol{b}$, which minimize Equation 2.44 with respect to $\boldsymbol{\beta}$. Hence, the regression coefficients become:

$$\boldsymbol{b} = \left(\boldsymbol{X}^T \boldsymbol{X}\right)^{-1} \boldsymbol{X}^T \boldsymbol{y} \tag{2.45}$$

Finally, the RSM is found from Equation 2.40 where $\boldsymbol{\beta} = \boldsymbol{b}$. The RSM can be verified against new simulation data. Additionally, the Goodness-of-Fit can be evaluated for several statistics, such as the Root Mean Squared Error (σ_e) or the Adjusted R-squared (R^2_{adj}) defined as:

$$\sigma_e = \sqrt{\frac{1}{m} \sum_{i=1}^{m} \left(e^{(i)}\right)^2} \quad , \quad \left(e^{(i)}\right)^2 = \left\| \frac{\hat{y}^{(i)} - y^{(i)}}{y^{(i)}} \right\| \tag{2.46}$$

$$R^2_{adj} = 1 - \frac{\sum_{i=1}^{m} \left(y^{(i)} - \hat{y}^{(i)}\right)^2}{\sum_{i=1}^{m} \left(y^{(i)} - \bar{y}^{(i)}\right)^2} \cdot \frac{m-1}{m-p} \tag{2.47}$$

$\bar{y}$ is the empirical mean of the sampled targets. A well fitted model is characterized by a Root Mean Squared Error close to 0 and an Adjusted R-squared coefficient close to one.

Chapter III

Previous work

■ This chapter presents the historical lines of draft tube development and previous work of draft tube optimization.

DTs were developed in connection with the emergence of reaction turbines in the first half of the 19th century [17]. The first one consisted of a cylindrical pipe, which allowed the turbine to be placed above the tailwater without losing any head [5]. Later on, the development of straight diffuser DTs increased the efficiency of the hydropower plants by slowing down the flow and recovering the pressure. The first DTs restricted the runner diameter to be small since larger runner diameters require long diffusers, and long diffusers increase the construction costs. The bell-mouth DT partially solved this problem. It has a diffuser shape with curved walls. This shape improved the efficiency of the DT when operating outside of design conditions, as it allowed for higher swirl and more pressure recovery per length. Moody improved this design with a cone filled center, which fills up the space of a dead zone in the water when operating in off-design conditions.

It was not before Kaplan developed the curved DT that runner diameters up to $10m$ were possible. The drawback of this design is that the DT performance is reduced compared to the previously discussed types, because of hydrodynamic losses in the bend. The benefit of higher power output from larger runners makes curved DTs commonly used today.

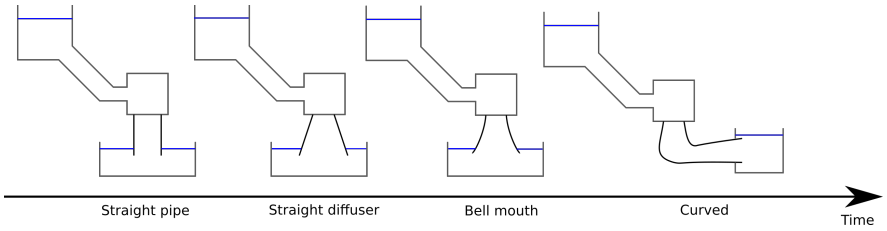

Figure 3.1: Draft tube type development through the times

Traditionally, DTs have been designed based on analytic methods, heuristics, and model tests [17]. The general shape of a DT is a diffuser and the inverse design method by Clabuk and Modi [31] and derivative-based optimization by Madsen [32] represent early approaches for diffuser designs.

Today, computational fluid dynamics (CFD) is a commonly used tool in DT design development, due to its benefits of flexibility and cost-effectiveness. However, CFD calculations can be time-consuming, so design development is commonly done by combining CFD with optimization algorithms. Marjavaara describes how Surrogate Models can be utilized as a tool for CFD driven optimization of DTs[5].

DT optimization studies commonly use C_p, [22, 33–37] and ξ [22, 33, 35, 37] as objectives. The goal of a optimization is always to increase C_p and decrease ξ to achieve higher DT performance. Economic perspectives may also be emphasized by considering the DT size as an objective [23]. Excavating and material consumption influence the civil costs, which again depend on parameters such as the DT volume, surface area and overall length dimensions. Hence, if a size dimension is chosen as an optimization objective, it is reduced to limit civil costs.

C_p are defined in Equation 2.13 with discharged averaged surface integrals in the nominator, whereas several studies rather use area averaged surface integrals [22, 33, 34, 36]. Thus the predictions of C_p would be slightly different, but not change the fact that C_p should be increased to achieve higher DT performance. In subsection 2.1.3 the definitions of C_p and ξ accounts for potential height variations between the DT inlet and outlet. However, several optimization studies excludes potential height from the analysis, whereas gravity forces are not considered in the CFD simulations [22, 33–37].

Accurate flow predictions in the DT is computationally expensive due to complex and unsteady flow. For instance, simulating the rotating vortex rope requires a very fine mesh and a sophisticated turbulence model [38]. However, when considering averaged characteristics such as the C_p and ξ, moderate meshes and more simple

turbulence models are assumed to be accurate enough [39]. Hence, DT optimizations are typically performed with steady-state RANS-equations together with $k - \epsilon$ or SST turbulence models [15, 37]. Optimization studies are commonly done by investigate the DT performance as a separate entity of the hydropower plant [22, 33–37]. The flow condition in the DT is highly dependent on the OP of the turbine. Hence, the BC must provoke the OP of interest. Several studies choose OP close to BEP [40], as optimization performed by McNabb consider 9 different OPs [23].

Coupled runner and DT optimization was performed by Lyutov [15]. This enables more accurate flow modeling at the runner-DT interface. The trade-off is increased computational effort with a larger computational domain. The study also optimized the runner alone and compared the resulting turbine efficiencies. The conclusion drawn showed advantages of simultaneously DT and Runner optimization in terms of 0.3% higher efficiency.

The number of DVs typically depends on if the purpose of the optimization. The runner outlet dimensions typically fix the inlet dimensions of the DT. When upgrading an already existing hydropower plant, the total height and length of the DT will typically be fixed, due to previously excavation work. Marjavaara and Lundström performed a redesign of the DT in Yngerdsforsen hydropower plant in Sweden, where three design variables were chosen [22]. Shojaeefard performed a DT optimization with only two parameters, for an already existing lab turbine at the Iranian Research Organization for Science and Technology [35]. For new design development, it is an advantage to keep the variable number high to explore more designs. However, more DVs would also be more computationally expensive. Lyutov states that 5-12 is the typical amount of DVs used for curved DT optimizations [15].

To the best of the Author's knowledge, design optimization of DTs in VSO hydropower plants has never been done. However, the main strategies of DT optimization performed on traditionally synchronous speed operating hydropower plants are applicable for this work.

Chapter IV

Method

■ This chapter presents the methodology of the work. It describes how the parametric design of the draft tube is constructed and how the mesh is generated. Furthermore, it defines how the optimization study is performed and how various uncertainties are investigated.

4.1 Software

This work is performed with the software ANSYS 2020 R1 and MATLAB R2020a. ANSYS SpaceClaim is utilized to create the DT geometry, ANSYS Meshing and ANSYS TurboGrid for meshing, ANSYS CFX for CFD calculations and ANSYS Workbench for organizing the parametric optimization study. MATLAB is further utilized for RSM and searches for improved design.

4.2 Full Simulation and Partial Simulation

Simulations are both performed of the DT alone and the DT together with GVs and the runner. The simulations performed with GVs and the runner are referred to as Full Simulations (FS), and the simulations performed with only the DT are referred to as Partial Simulations (PS). The DT design DT_i utilized for FS or PS are indicated with index notation FS_i or PS_i

A PS is less computationally expensive compared to FS as the computational domain is reduced. Hence, the optimization simulations are performed as PSs, but FSs are done to provide BC at the DT inlet for the PS. BC_i denotes BC obtained from FS with DT_i.

4.3 Geometric Parameterization

11 geometric parameters (GPs) are chosen to parameterize the DT geometry. Ansys SpaceClaim is utilized to build the geometry. A script written in the Python programming language imports the GPs, and calculates the points: $P_i, i = 0, 1, 2, 3, 4, 5$, shown in Figure 4.1. These points define the meridian line of the DT. Cross-sections are drawn at positions along the line with spline curves, which are lofted into volumes. The DT is divided into segments to more easily control the mesh in different regions. The script also creates *Named Selections* of surfaces and segments, which work as identifications for further addressing the mesh and simulation set-up. The entire DT construction script is appended as an electronic attachment. The black-colored variables denote GPs of the optimization as grey-colored variables are derived from the GPs or fixed for the optimization in Figure 4.1, Figure 4.2, Figure 4.3, and Figure 4.5.

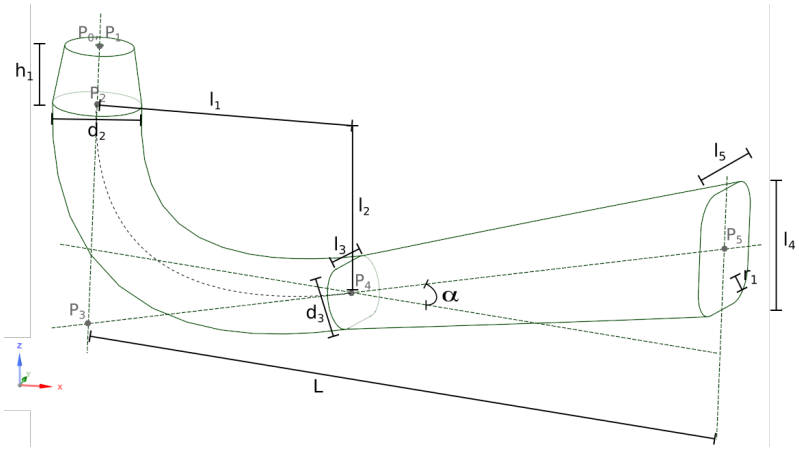

Figure 4.1: The geometric parameterization of the draft tube.

4.3.1 The Cone

The DT inlet is fixed to ensure that it always matches the runner outlet. d_0 represents the diameter of the runner hub facing the DT tube. The water enters the DT within the diameter d_1 through an inclined surface of height h_0 around the hub. The cone geometry is circular and diverging with a linear increase of the diameter d. The GP h_1 defines the length of the cone, and the GP d_2 defines the diameter of the cone outlet. The cone geometry is illustrated in Figure 4.2, and the corresponding variables and geometric relations are summarized in Table 4.1.

Variable	Value	Explanation
h_1	GP	Cone height.
d_2	GP	Diameter of the cone outlet.
P_0	$[0, 0, -171]$	Center point of the runner hub wall.
P_1	$P_0 - h_0\hat{k}$	Center point of the cone inlet.
P_2	$P_1 - h_1\hat{k}$	Center point of the cone outlet.
d	$d_1 + (d_2 - d_1) \cdot t$	Cross-sectional diameter in the cone.
d_0	$40.00mm$	Fixed diameter of the runner hub wall.
d_1	$350.09mm$	Fixed diameter of the DT inlet.
h_0	$8.13mm$	DT inlet height.

Table 4.1: Geometric variables and relations in the cone, $t \in [0, 1]$.

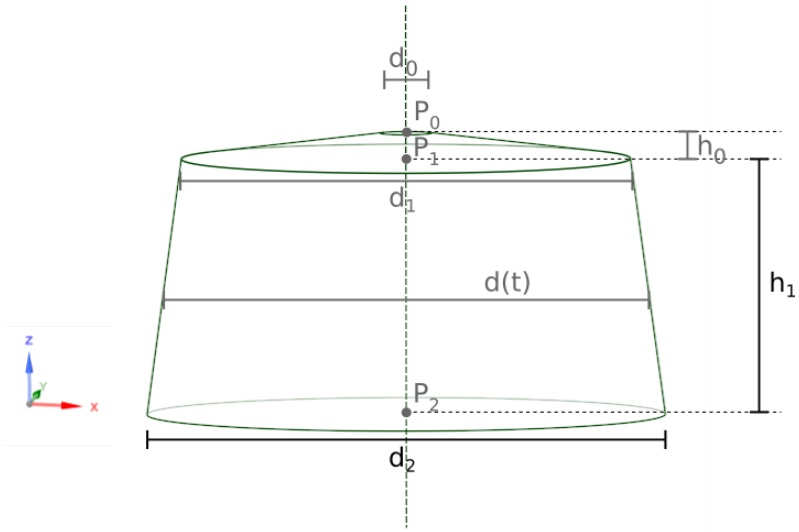

Figure 4.2: The geometric parameterization of the cone.

4.3.2 The Elbow

A quadratic Bézier curve defines the centerline of the elbow. The curve starts in P_2, ends in P_4, and has a control point in P_3. Figure 4.3 illustrates how the elbow is constructed by sketching 20 cross-sections along the centerline. Planes are created perpendicular to the Bézier curve by using the derivative in locations along it as the normal vector.

The cross-sectional area shape is changed from circular at the inlet of the elbow to rectangular with two opposing straight and bowed sides at the outlet. The GP d_2 defines the diameter of the elbow inlet. The GPs l_3 and d_3 define the length of the straight sides and the diameter of the bowed sides of the elbow outlet. The orientation of the elbow outlet is defined by the GP α, which denotes the angle between the outlets normal vector and the horizontal plane. The cross-sections throughout the elbow are described with the two parameters; l and r. l is increased linearly along the Bézier curve from 0 at the inlet to $\frac{l_3}{2}$ at the outlet. r is adjusted so that the cross-sectional area follows the relationship in Figure 4.4, inspired by Figure 2.7. Hence, the elbow is slightly contracted at the end to reduce flow separation due to the curved wall. Variables and geometric relations in the elbow are summarized in Table 4.2.

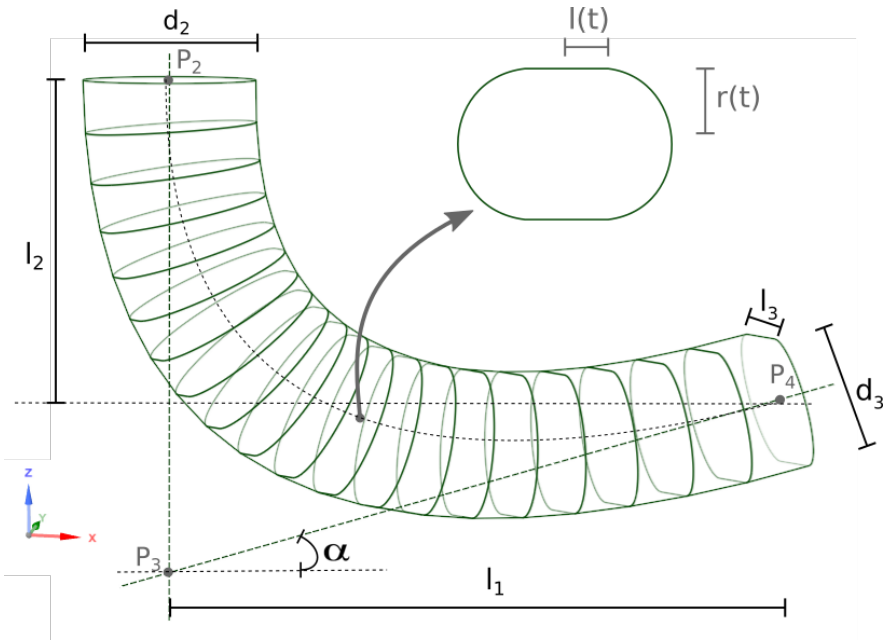

Figure 4.3: The geometric parameterization of the elbow.

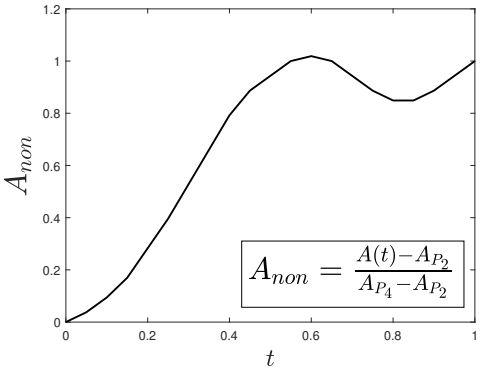

Figure 4.4: Nondenominational area relation in the elbow. A_{P_2} denote the area of the elbow inlet, A_{P_4} is the area of the elbow outlet and $A(t)$ is the cross-sectional area along the elbow center line parameterized by $t \in [0, 1]$.

Variable	Value	Explanation
d_2	GP	Diameter of the cone outlet.
l_1	GP	Horizontal length of the elbow.
l_2	GP	Vertical length of the elbow.
d_3	GP	Diameter of the elbow outlet.
l_3	GP	Length of straight sides of the elbow outlet
α	GP	Angle between the normal vector of the elbow outlet and the horizontal plane.
P_2	$P_1 - h_1\hat{k}$	Center point of the elbow inlet.
P_3	$P_2 - (l_2 + l_1 \cdot sin(\alpha))\hat{k}$	Control point of the Bézier curve.
P_4	$P_2 + l_1\hat{i} - l_2\hat{k}$	Center point of the elbow outlet.
A	$A(t)$	Cross-sectional area of the elbow.
l	$\frac{l_3}{2} \cdot t$	Cross-sectional parameter.
r	$\frac{2l}{\pi} \cdot \left(\sqrt{1 + \frac{A}{4\pi l^2}} - 1\right)$	Cross-sectional parameter.

Table 4.2: Geometric variables and relations in the elbow, $t \in [0, 1]$

4.3.3 The Exit diffuser

The exit diffuser is built of 15 cross-sections along the straight centerline between P_4 and P_5, illustrated in Figure 4.5. The orientation of the outlet is held fixed, parallel with the yz-plane. The orientation of the inlet is dependent on the GP α. Hence, the orientation of each cross-section sketched throughout the exit diffuser is linearly changed.

The inlet is defined by the GPs l_3 and d_3, and the outlet is defined by the GPs l_4, l_5 and r_1. The total length of the exit diffuser is defined by $L - l_1$. The cross-sections throughout the exit diffuser are defined by the parameters h, b, and r. They change linearly from the inlet to the outlet of the exit diffuser, more detailed explained in Table 4.3.

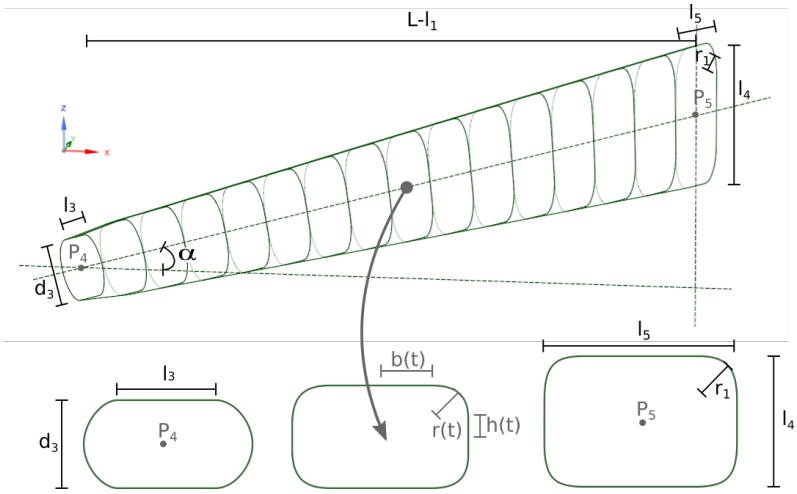

Figure 4.5: The geometric parameterization of the cone.

Variable	Value	Explanation
d_3	GP	Diameter of the exit diffuser inlet.
l_3	GP	Length of straight sides of the exit diffuser inlet.
α	GP	Angle between the normal vector of the exit diffuser inlet and the horizontal plane.
L	GP	Horizontal length of the entire DT.
l_4	GP	Height of the DT outlet.
l_5	GP	Width of the DT outlet.
r_1	GP	Radius of the outlet corners.
P_4	$P_2 + l_1\hat{i} - l_2\hat{k}$	Center point of the exit diffuser inlet.
P_5	$P_4 + (L - l_1) \cdot cos(\alpha)\hat{i} + (L - l_1) \cdot sin(\alpha)\hat{k}$	Center point of the DT outlet.
b	$\frac{1}{2}(l_3 + (l_5 - 2r_1 - l_3) \cdot t)$	Cross-sectional parameter.
h	$(l_4 - 2r_1) \cdot t$	Cross-sectional parameter.
r	$r_1 \cdot t$	Cross-sectional parameter.

Table 4.3: Geometric variables and relations in the elbow, $t \in [0, 1]$.

4.4 Mesh generation

The resulting DT geometry consists of 15 volume segments, illustrated in Figure 4.6. The segments have their meshes generated in a specific order listed in Table 4.4. A *Shared Topology* procedure is applied to neighbouring segments. This makes the mesh generated for one segment a boundary for the subsequent segment, ensuring compatible mesh interfaces at the seams.

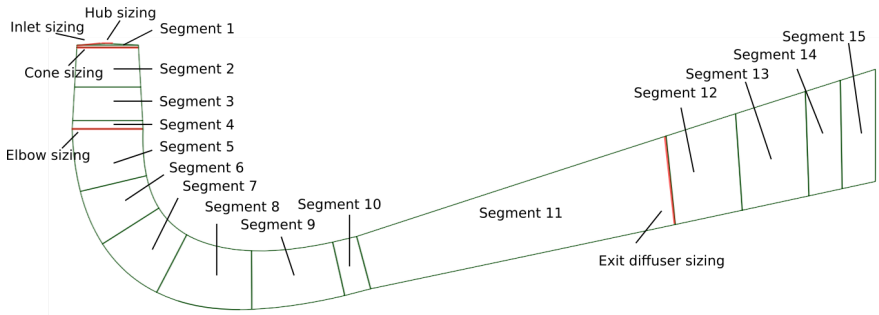

Figure 4.6: Segments and interfaces of the mesh set-up.

Most of the segments are meshed with *Multizone Method*. This is a sweeping meshing algorithm providing a hexahedral mesh. The length of the elements in the merdian direction is controlled separately for each segment by the *sweep element size*. The segments in the transition between the cone and the elbow and the elbow and the exit diffuser are meshed with *Patch Conforming Method*. This method provide unstructured tetrahedral elements, enable the number of elements in the cross-section perpendicular to the flowing direction to change throughout the segment. The number of mesh elements in the cone, the elbow, and the exit diffuser is controlled by *Face Sizing* at one cross-section in each part. The element sizing is specified at the red marked faces in Figure 4.6.

Segment 1 is meshed with the *Patch Conforming Method*, as the *Multizone Method* worked poorly due to the inclined surface of the DT inlet. The element size is controlled at both the inclined surface where the water is entering the DT and at the runner hub interface wall.

10 inflation layers are applied to increase the mesh resolution close to the wall. The inflation layers are specified with the first layer thickness and the growth rate of the distance between each layer. The growth rate is kept by the default value of 1.2 for all segments. The first layer thickness is slightly increased for the segments in

the elbow compared to the segments in the cone, and even further increased for the segments in the exit diffuser. The inflation layers in the transition segments between the cone, the elbow, and the exit diffuser are applied smooth transition setting rather than first layer thickness, to ensure that the mesh is gradually changed between the different parts of the DT.

The mesh resolution is higher in the cone, where the flow is more complex. The element size is gradually increased throughout the segments from the cone to the beginning of the exit diffuser. The mesh resolution is gradually increased in the meridional direction of the exit diffuser to ensure better BC modeling at the DT outlet. The mesh is coarser in some parts to limit the computational cost. The mesh settings for all the segments and interface sizing are summarized in Table 4.4 and Table 4.5.

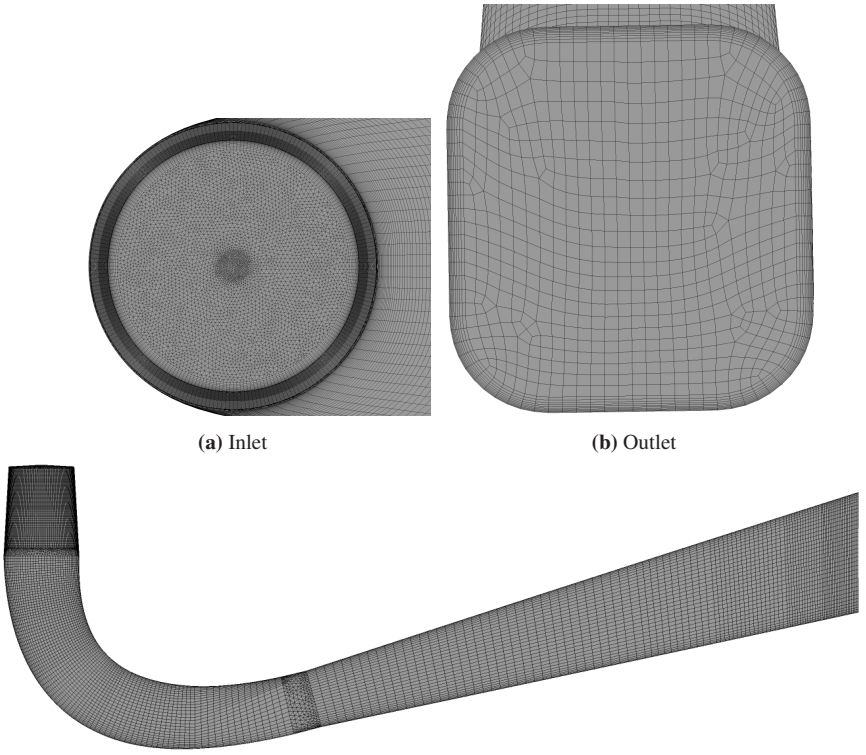

(a) Inlet **(b)** Outlet

(c) Side view

Figure 4.7: Mesh generated on the reference draft tube.

Segment	Mesh method	Inflation layer	Update Order
1	Patch Conforming	FLT: 0.5mm	13
2	Multizone, 7.0mm	FLT: 0.5mm	1
3	Multizone, 10.0mm	FLT: 0.5mm	2
4	Patch Conforming	Smooth transition	14
5	Multizone, 15.0mm	FLT: 0.6mm	3
6	Multizone, 20.0mm	FLT: 0.6mm	4
7	Multizone, 25.0mm	FLT: 0.6mm	5
8	Multizone, 30.0mm	FLT: 0.6mm	6
9	Multizone, 40.0mm	FLT: 0.6mm	7
10	Patch Conforming	Smooth transition	15
11	Multizone, 50.0mm	FLT: 1.0mm	8
12	Multizone, 40.0mm	FLT: 1.0mm	9
13	Multizone, 25.0mm	FLT: 1.0mm	10
14	Multizone, 15.0mm	FLT: 1.0mm	11
15	Multizone, 1.0mm	FLT: 1.0mm	12

Table 4.4: Mesh method, inflation layer settings and update order for the segments of the DT geometry. The length value of Multizone method denotes the sweep element size. FLT denotes the first layer thickness of the inflation layers.

Interface	Element size
Hub	2mm
Inlet	5mm
Cone	5mm
Elbow	15mm
Exit Diffuser	20mm

Table 4.5: Interface sizing settings of the mesh. Interfaces are illustrated in Figure 2.8

It should be noted that a mistake was made with the inflation layer setup in the optimization study. Segment 5 were specified to only have 5 inflation layers, and not 10 as the rest of the segments. The amount of inflation layers specified for a segment only puts an upper bond of inflation layer the meshing algorithm will produce. Since segment 5 was the first segment to be meshed in the elbow, the entire elbow was meshed with only 5 inflation layers. This error caused the mesh algorithm not to work for several DT geometries . Additionally, it was discovered too late to do the entire optimization study all over. A more detailed description of which DT designs that were present for this mistake is described in subsection 5.3.1 and a reflection of how this affected the optimization study is described in section 6.2.

4.5 Guide vanes and Runner mesh

This study reuses the meshes of the GVs and runner utilized by Ilievs [**?**].The meshes of the flow passages around a GV and a runner blade is built in ANSYS TurboGrid. The meshes provided consist of purely hexahedral elements. As the GV opening varies with the turbine OP, the mesh of the GV passage is different for each OP.

The turbine configuration consists of 28 GVs and 17 runner blades. The entire geometry is built by doing a mesh transformation in ANSYS CFX-Pre. The meshes of the GV passages and runner blade passages are copied and rotated around the center axis of the turbine. The final mesh is illustrated in Figure 4.8.

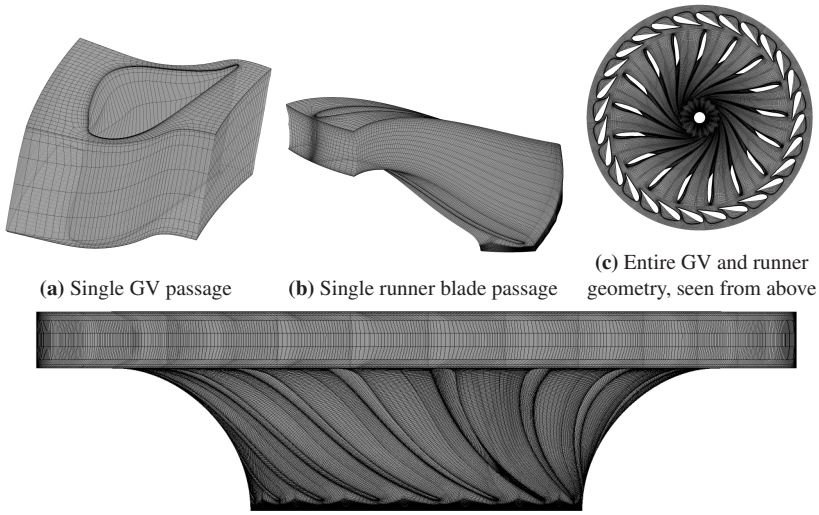

(a) Single GV passage

(b) Single runner blade passage

(c) Entire GV and runner geometry, seen from above

(d) Entire GV and runner geometry, side view

Figure 4.8: Mesh of the guide vanes and the runner.

4.6 Optimization study

Three OPs corresponding to PL, BEP, and HL are considered for the analysis. An overview of the runner speed, discharge, GV openings, and head of the different OPs is shown in Table 4.6.

OP	**Runner speed** $[rpm]$	**Discharge** $[m^3/s]$	**GV opening** $[^\circ]$	**Head** $[m]$
PL	338.40	0.10577	5.535	12.0
BEP	348.43	0.19066	10.000	12.0
HL	351.70	0.22477	12.076	12.0

Table 4.6: Operation points of the optimization.

The optimization is preformed as an SBO analysis. Two main objectives are chosen, namely the pressure recovery factor (C_p) and the DT volume (V). Four RSMs are built for predicting C_p at each of the three OPs and V. C_p is defined to be calculated as:

$$C_p = \frac{\frac{1}{Q}\int_{out} P(\vec{v}\cdot d\vec{S}) - \frac{1}{Q}\int_{in} P(\vec{v}\cdot d\vec{S})}{\frac{1}{2}\rho\left(\frac{Q}{A_{in}}\right)^2} \tag{4.1}$$

It should be noted that potential height z is excluded from the definition of C_p in Equation 4.1 compared to the previous definition from the theory in Equation 2.13. The reason is that z will not contribute to a static pressure gradient in the simulations because gravity forces are excluded.

4.6.1 Design Space

The design space in terms of GPs is presented in Table 4.7. Central values (CVs) of the GPs are found from measuring $\text{DT}_{Francis\,99}$. The parameterization and design constraints described in section 4.3 generates a DT which looks quite similar, but not identical to $\text{DT}_{Francis\,99}$. The DT generated by the CVs of the GPs is referred to as DT_{ref} throughout the text.

The design space was first suggested to be within $\pm 30\%$ of the CVs. The percentage range was further reduced for d_2, l_3, l_4, l_5, d_3 and r_1. This was done to ensure that all possible DT designs have an increased cross-sectional area from the DT inlet to the outlet. Hence, a diffuser shaped DT will always be produced. The design space was also reduced to ensure that the mesh algorithm works.

DV	x_1	x_2	x_3	x_4	x_5	x_6	x_7	x_8	x_9	x_{10}	x_{11}
GP	$h_1[mm]$	$l_1[mm]$	$l_2[mm]$	$\alpha[^\circ]$	$L[mm]$	$d_2[mm]$	$l_3[mm]$	$l_4[mm]$	$l_5[mm]$	$d_3[mm]$	$r_1[mm]$
LL	334	1021	533	13.0	3062	364	263	511	470	293	144
CV	477	1459	761	15.0	4374	404	277	636	588	308	160
UL	620	1897	989	17.0	5686	444	291	761	706	323	176

Table 4.7: Design space for the optimization. The abbreviation of the first column denotes DV: design variable, GP: geometric parameter, LL: lower limit, CV: center value and UL: upper limit.

Notably, l_4 equals 639mm at DT$_{Francis\,99}$. By an accident, the value of 636mm was used as the center value for the optimization.

For the simulations, the GPs are taken as input for geometry generation, as for the RSM, non-dimensional DVs are utilized. The design space of all DVs are $x_i \in [-1, 1]$. A GP and its corresponding DV is by this related as:

$$x_i = \frac{\text{GP}_i - \text{GP}_{CV_i}}{\frac{1}{2} \cdot (\text{GP}_{UL_i} - \text{GP}_{LL_i})} \tag{4.2}$$

4.6.2 Design of Experiment

BBD is chosen as the DOE method. For 11 DVs, BBD is built with 11 blocks with 16 factorial parts per block. This makes up a total of 176 different combinations of the design variables. Additionally, the center point must be added, creating 177 different designs that are simulated for each OP. For the RSM, the center point is added 11 extra times to facilitate rotatability.

4.6.3 CFD set up

The simulation setup in ANSYS CFX is summarized in Table 4.8. Several modeling assumptions are made to provide simulations that would be computationally possible within the time limits of the work and the resources available. As a trade-off, these assumptions might introduce modeling errors. However, the goal of the optimization is not to obtain a highly accurate solution of the flow field, but to capture the most important trends so that C_p can be predicted with sufficient precision.

	Parameter	Description
General	Analyse type	RANS, steady state
	Discretization	Advection scheme: High Resolution Turbulence numeric: High Resolution
	Turbulence model	$k-\epsilon$ model with scalable wall function, 5% intensity at the inlet of the domain
	Convergence criteria	RMS of: continuity, momentum, pressure and turbulence quantities $\leq 10^{-4}$
	Temperature	19°C
	Assumptions	Incompressible, Single-phase, Adiabatic, No gravity force
	Solver accuracy	Double precision
FS	Boundary condition	Inlet: Mass flow rate with normalized velocity direction ($c_r = -0.458589$, $c_\theta = -0.888649$, and $c_z = 0$) Outlet: Average static pressure equal zero Walls: No slip condition, smooth walls
	Domain interface	Frozen Rotor
	Time scale factor	Linear increase the first 600 iterations from 1 to 7, then kept constant at 7.
	Iterations	Minimum: 1200, Maximum: 1500
PS	Boundary condition	Inlet: Velocity magnitude and direction Outlet: Average static pressure equal zero. Walls: No slip condition, smooth walls
	Time scale factor	Constant, 0.5 for PL and BEP and 0.1 for HL
	Iterations	Minimum: 400 for PL and BEP, 500 for HL Maximum: 600 for PL and BEP, 700 for HL

Table 4.8: Simulation setup in ANSYS CFX.

The optimization simulations are performed as PSs, but FSs are utilized to obtain BCs of the DT inlet. The velocity profile at the runner-DT interface is exported from FS_{ref} of each OP, and utilized as inlet BC for all PSs. Hence, only one costly FS is needed, as 177 less costly PSs are performed in the optimization of each OPs.

The inlet BC of FSs is given as the mass flow rate of the OP. The flow is assumed to enter the GVs in a uniform direction, corresponding to the outlet direction of the flow in the stay vanes passages of the reference design. The outlet BC is static, average pressure equal to 0, and walls are given no-slip condition for both PSs and FSs. The domain interface of the FSs is modeled as a Frozen Rotor. The runner domain and the hub wall in the DT domain are specified to rotate with the runner speed corresponding to the OP.

The simulations are calculated as steady-state using the $k-\epsilon$ model for modeling turbulence. High resolution are chosen for the advection scheme and the turbulence

numeric. The water temperature equals 19°C, and the flow is assumed to be adiabatic, incompressible, and single-phase. Hence, modeling cavitation is impossible with this setup and, therefore, neglected from the analysis.

Gravity forces are excluded from the analysis. This is feasible even though the flow in an actual hydropower plant is driven by gravity forces, as the CFD flow is driven by BCs. However, if the C_p predicted by the CFD calculations is validated against experimental data, the presence of the hydrostatic pressure in the experimental data must be taken into account.

A time scale factor is applied to control the speed of convergence in the simulations. Its value is found by trial and error until the simulation convergences with sufficient time without fluctuating behavior of the residuals. The timescale factor imposed at the FSs is increased linearly from 1-7 over the first 600 iterations and kept constant at 7 for the remanding ones. For the PSs, the timescale factor is kept constant, equal to 0.5, for PL and BEP simulations and 0.1 for HL simulations. A convergence criterion is defined to be Root Mean Square (RMS) of the residuals of $RMS \leq 10^{-4}$. The number of iterations is chosen by trial and error testing of FS_{ref} and PS_{ref} until sufficient convergence is achieved. As the timescale factor is chosen to be lower for PS at HL, compared to PS at PL and BEP, the number of iterations is slightly higher. All simulations are solved with double precision in the solver.

4.6.4 Objective calculations

The objectives are calculated in ANSYS CFX Post with the CFX Expression Language (CEL). The integrals of C_p defined in Equation 4.1 are calculated with the command $massFlowAve()@$, which predicts a mass flow averaged integral. When modeling flow with constant density, the results become the same as a discharged averaged integral. Written in CEL, the objectives are calculated as:

```
Cp = (massFlowAve(Pressure)@dt_outlet -
     massFlowAve(Pressure)@dt_inlet)/
     (0.5*Density*(massFlow()@dt_inlet/
     Density/area()@dt_inlet)^2)

V  = volume()@DT
```

dt_inlet, *dt_outlet* and *DT* are defined in CFX Pre as the surfaces of the DT inlet, outlet and the entire DT domain. CEL is also utilized to evaluate y^+ values and mesh metrics during the simulations.

4.6.5 Response surface modeling and new design exploration

4 response surfaces are built in total, one for C_p and at each OP and one for V. All the RSM and design exploration is performed in MATLAB. Several built-in functionalities from the Curve Fitting Toolbox are utilized. The RSMs are built-in MATLAB with the function $fitlm()$. By using the model specification $'quadratic'$, it returns a second-order regression model built by fitting the input data with least square minimization of the error. The input data is a matrix of the DVs and their corresponding simulation results of the objectives. The script utilized for RSM is appended as an electronic attachment.

The accuracy of the response surfaces is evaluated with the Goodness-of-Fit indicators σ_e and R^2_{adj}. Sensitivity analyses of the response surfaces are performed by utilizing the function $rstool()$. The analyses indicate how the DT performance depends on each DV individually.

The function $predict()$ is further utilized to predict responses of new designs. The function takes in a linear regression model object and an array of DVs as an input and returns a predicted response as an output. 100 millions (M) random designs are evaluated for each objective. The designs are divided into 10 batches of 10M each to not run out of memory when predicting the responses.

Pareto fronts are used to visualize possible improvements of C_p and V simultaneously, for each OP. A search for optimal designs is performed by sorting out all designs with all four objectives, equal or improved, compared to DT_{ref}. The maximum improvement of each objective individually is further searched for in this population. Finally, a design that considers improvements in all four objectives simultaneously is found.

4.7 Verification and validation

The accuracy of the optimization simulations is verified in several ways. The modeling of the turbulent BL near the wall is considered by investigating the y^+ value. Mesh metrics of the aspect ratio, orthogonal angle, volume expansion, and mesh quality are checked.

A GCI analysis of C_p is performed for each OPs to evaluate the numerical accuracy of the mesh. DT_{ref} is utilized as the geometry, and the medium-resolution mesh is achieved with the mesh settings used in the optimization simulations. The coarser and the finer meshes are generated by tweaking sizes defined in the settings of the medium resolution mesh. However, the first layer thickness of the inflation layers is kept constant for all mesh resolutions. An overview of all the mesh settings applied for generating the mesh is presented in Appendix C.

Possible modeling errors introduced by excluding the GVs and the runner from the simulations are investigated. This analysis is further referred to as *DT inlet BC test*.

Validation of the CFD results is impossible because the optimization study investigates new DT designs. Hence, there exists no experimental data to compare with the simulations. However, the optimized DT designs predicted by the RSMs, are verified with PS and FS.

4.7.1 Draft tube inlet boundary condition tests

Excluding the runner and GVs from the optimization-simulations might lead to modeling errors. The velocity profile imposed at the DT inlet is a stiff BC, which is assuming the flow field to be fixed. Additionally, the velocity profile at the runner-DT interface is assumed to be equal for all DT designs by excluding the runner and the GVs from the analysis. The elliptic nature of the governing equations can further cause the potential errors introduced at the DT inlet to propagate into the DT domain. To investigate how much this affects calculations of C_p, two types of analyses are performed. Since V is purely dependent on the geometry and not the flow condition, it is not considered by the BC uncertainty analysis.

Three different DT designs are considered for the analysis, respectively DT_{ref} and two other designs, denoted DT_a and DT_b. Compared to DT_{ref}, DT_a is smaller and more diverging, and DT_b is larger and less diverging. Table 4.9 shows the GPs of DT_a and DT_b.

	$h_1[mm]$	$d_2[mm]$	$l_1[mm]$	$l_2[mm]$	$d_3[mm]$	$l_3[mm]$	$l_4[mm]$	$l_5[mm]$	$L[mm]$	$r_1[mm]$	$\alpha[^\circ]$
$\mathbf{DT}_a$	335	404	1021	533	308	277	639	588	3062	160	10.5
$\mathbf{DT}_b$	620	404	1896	989	308	360	447	588	5685	112	15

Table 4.9: Geometric parameters of DT_a and DT_b.

The first test investigates the difference between doing a FS versus a PS with the same DT design. The inlet BC for the PS is obtained by exporting the velocity profile from the runner-DT interface in the FS. The first test can be expressed as comparing simulations of:

$$\text{FS}_i \text{ vs. } \text{PS}_i \text{ with } \text{BC}_i \quad i = ref, a, b \tag{4.3}$$

The second test investigates the effect of using different inlet BCs. PS simulations are performed for each DT design with inlet BC achieved from FS of all three DT designs. The second test can be expressed as comparing simulations of:

$$\text{PS}_i \text{ with BC}_i \text{ vs. PS}_i \text{ with BC}_j \quad i,j = ref,a,b \quad i \neq j \tag{4.4}$$

The CFD setup is the same as for the optimization study. The tests are performed for all OPs. It should be noted that the analysis was performed early in the work when a larger design space was considered. This is the reason why some of the GPs of DT_a and DT_b exceed the design space of the optimization study.

Chapter V

Results

■ This chapter presents all results of the research. The first section evaluates the mesh in terms of y^+, mesh metrics, and GCI. The second section presents the key findings from the DT inlet BC tests. The last section describes the results of the optimization study. An evaluation of the response surfaces is shown in terms of the Goodness-of-fit indicators and the sensitivity plots. The strategy of finding optimized designs is described, and five candidates for improved designs are suggested. Scripts and simulation results are attached to the thesis as electronic attachments, but an overview of the files is presented in Appendix E.

5.1 Mesh

The quality of the mesh is presented in terms of y^+ values, mesh metrics parameters, and the GCI analysis. The GV and the runner are not considered in the mesh quality analysis, whereas they are previously discussed by Iliev [11].

5.1.1 y^+ values

Table 5.1 summarizes the averaged values of y^+, achieved from all the optimization simulations for each OP.

	$PL_{5\,IL}$	$PL_{10\,IL}$	$BEP_{5\,IL}$	$BEP_{10\,IL}$	$HL_{5\,IL}$	$HL_{10\,IL}$
Average	86.74	62.1	65.4	50.1	70.9	54.1
Minimum	18.1	16.5	16.9	15.2	18.6	16.4
Maximum	312.5	143.7	214.2	131.0	279.2	120.8

Table 5.1: y^+ values achieved from the optimization simulations at different OPs. The subscript $5IL$ and $10IL$ denotes simulations performed with 5 and 10 inflation layer in the elbow.

5.1.2 Mesh metrics

Table 5.2 summarizes the averaged values of different mesh metrics obtained from the optimization-simulations performed at PL. The mesh metrics are assumed to be equal for all OPs since the same meshing algorithm is utilized for all OP.

Parameter	**Value**$_{5\,IL}$	**Value**$_{10\,IL}$	**Recommended**
Aspect ratio	Average: 7 Max: 75	Average: 9 Max: 85	<1000
Orthogonality angle	Average: 82.6° Min: 16.9°	Average: 83.1° Min: 31.3°	>20?
Volume expansion	Average: 2 Max: 4350	Average: 2 Max: 185	<20
Mesh quality	Average: 0.62 Min: 0.02	Average: 0.59 Min: 0.02	Range: 0-1, 1 is ideal
Amount of elements	$8.4 \cdot 10^5$	$8.9 \cdot 10^5$	-
Amount of nodes	$6.5 \cdot 10^5$	$6.9 \cdot 10^5$	-

Table 5.2: Average mesh quality parameters obtained from the optimization simulations with 5 and 10 inflation layers in the elbow.

5.1.3 GCI results

The results from the GCI analysis are presented in Table 5.3. The analysis shows approximately a factor of 10 higher GCI index values of PL, compared to BEP and HL. For the optimization simulations, the medium resolution mesh is utilized. Thus the value of $GCI^{C_p}_{medium}$ indicates the grid convergence of the simulations performed at each OPs.

	PL	**BEP**	**HL**
$(N_1, N_2, N_3) \cdot 10^5$ [−]	26.32, 8.95, 3.73	26.33, 8.96, 3.72	26.27, 8.95, 3.74
r_{21}, r_{32} [−]	1.4321, 1.3382	1.4319, 1.3398	1.4316, 1.3373
$C_{p\,1}, C_{p\,2}, C_{p\,3}$ [−]	1.2275, 1.2333, 1.2273	0.8471, 0.8449, 0.8426	0.8894, 0.8918, 0.8949
p [−]	0.1044	0.8359	1.3716
$C^{21}_{p,\,ext}$[−]	1.0757	0.8534	0.8856
e^{21}_{a} [%]	0.47	0.26	0.27
e^{21}_{ext} [%]	14.11	0.73	0.43
$C^{32}_{p,\,ext}$ [−]	1.4276	0.8534	0.8856
e^{32}_{a} [%]	0.49	0.28	0.34
e^{32}_{ext} [%]	13.61	0.99	0.70
$GCI^{C_p}_{fine}$ [%]	15.46	0.92	0.53
$GCI^{C_p}_{medium}$ [%]	19.69	1.25	0.87

Table 5.3: GCI results for each operation point.

5.2 Draft tube inlet boundary condition tests

C_p plotted along the meridional distance of DT$_{ref}$ for the test cases described in subsection 4.7.1, is shown in Figure 5.1. Similar plots are also achieved from simulations of DT$_a$ and DT$_b$ indicating the same trends observed for DT$_{ref}$. Plots of all designs are attached in Appendix D.

The first test case investigates the difference between doing an FS versus a PS of the same DT design. The plots to the left in Figure 5.1 show that FS gives a slightly higher C_p than PS. The difference is most present at PL, at the entrance of the DT. Besides the offset introduced at the DT inlet, C_p seems to follow the same pattern throughout the DT for PS and FS.

The second test-case investigates the effect of using different BCs achieved from FS of different DT designs at PSs of a fixed DT design. The different simulations results of C_p plotted along with the meridional distance of the DT is shown in the plots to the right in Figure 5.1. C_p is following approximately the same pattern for all simulations, except in a region of about 20-40% distance from the inlet at BEP and HL. A smaller offset is also observed for PL in the area around 40% of the meridional distance. However, at the DT outlet, C_p becomes approximately the same for all simulations.

An overview of the absolute relative errors observed between C_p for the various simulations performed are displayed in Table 5.4. A significant difference in C_p is observed for test 1, which is a factor of 10 higher for PL, compared to BEP and HL. Test 2 shows approximately no variation in C_p for PSs with different BCs.

	Test 1		Test 2		
	$\epsilon_{ref}^{(1)}$	$\epsilon_{ave}^{(1)}$	$\epsilon_{a}^{(2)}$	$\epsilon_{b}^{(2)}$	$\epsilon_{ave}^{(2)}$
PL	13.96 %	14.61%	0.08%	0.49%	0.23%
BEP	2.11%	1.95%	0.15%	0.13%	0.38%
HL	1.46%	1.51%	0.37%	0.24%	0.57%

Table 5.4: Absolute difference of C_p calculated for the DT inlet BC test. $\epsilon_{ref}^{(1)}$ denotes the absolute difference of PS and FS performed with DT$_{ref}$, as $\epsilon_{ave}^{(1)}$ denotes the averaged absolute difference for the same comparison also done with DT$_a$ and DT$_b$. $\epsilon_{a}^{(2)}$ denotes the absolute difference between PS$_{ref}$ with BC$_{ref}$ and BC$_a$, as $\epsilon_{a}^{(2)}$ denotes the absolute difference between PS$_{ref}$ with BC$_{ref}$ and BC$_b$. $\epsilon_{ave}^{(2)}$ denotes the averaged absolute difference of PSs performed of the designs DT$_{ref}$, DT$_a$, and DT$_b$ done with their respectively BCs and the other designs BCs.

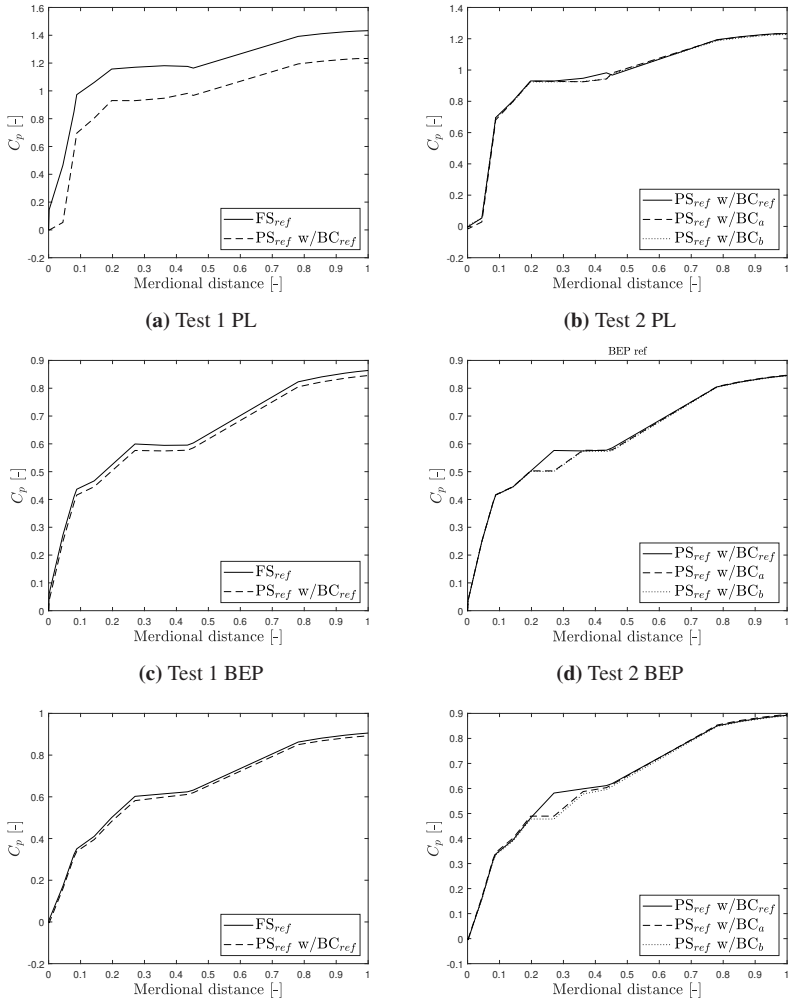

(a) Test 1 PL

(b) Test 2 PL

(c) Test 1 BEP

(d) Test 2 BEP

(e) Test 1 HL

(f) Test 2 HL

Figure 5.1: C_p plotted along the merdional distance of DT$_{ref}$ for the draft tube inlet boundary condition tests.

5.3 Optimization study

The optimization study was run as three separate parametric studies for each OP in ANSYS Workbench. The simulation results of the objectives at all DPs are appended as an electronic attachment. The simulations ran with 12 cores, and the CPU time was in the order of magnitude of 10^4 CPU seconds for each DP. In total, $3 \cdot 177 = 531$ simulations were performed.

5.3.1 Challenges with geometry and mesh generation

Several DPs failed with the message of incomplete geometry generation in ANSYS SpaceClaim. Investigation of the problem showed that the error was caused by the script generating the geometry hanging. When rerunning the failed DPs multiple times, the geometry generation eventually worked without any changes in the setup. However, this error increased the time needed to obtain the simulation results.

As previously mentioned in section 4.4 and section 5.1, an error in the mesh settings caused the elbow to be meshed with only 5 inflation layers. As a consequence, the mesh algorithm failed for several DPs, and no simulations were performed. In total, 22 out of 177 DPs failed for PL and HL, as 23 out of 177 DPs failed for BEP. When the inflation layer error was discovered, there was not enough time left to rerun all DPs. However, the failed DPs were rerun with 10 inflation layers in the elbow. Thus only 4 DPs failed for each OP.

5.3.2 Performance of the reference design

The objective values from simulations of the reference design DT_{ref} are displayed in Table 5.5. Optimized designs are discussed in terms of increased performance relative to this design. Response surfaces are built with simulation results from PS. Thus, predicted responses from the response surfaces are considered as improved if they obtain better scores in the objectives than PS_{ref} with BC_{ref}. Simulations of suggested improved designs are compared with both FS and PS results of DT_{ref}.

	$C_{p\,PL}[-]$	$C_{p\,BEP}[-]$	$C_{p\,HL}[-]$	$V[m^3]$
FS_{ref}	1.4330	0.8639	0.9058	1.1160
PS_{ref} w/BC_{ref}	1.2327	0.8446	0.8927	1.116

Table 5.5: PS and FS objective results of DT_{ref}. Optimized DT designs are discussed based on improvements in the objectives, meaning increasing C_p for each OP and decreasing V.

5.3.3 Response surface modeling

Response surfaces, RSM_A, were first built with the results obtained from the optimization-simulations with 5 inflation layers in the elbow. Once the error of the meshing was discovered, refined response surfaces, RSM_B were built, including the updated DPs with 10 inflation layers in the elbow. RSM_B was used for further discussion of optimized designs. In total, 78 regression coefficients are produced for each response surface, due to the 11 DVs.

Goodness-of-fit

The simulation results of the DPs with 10 inflation layers in the elbow, were compared against their respective predictions with RSM_A. The comparison showed an averaged absolute error of the differences relative the simulated results of 1.9% for $C_{p\,PL}$, 0.6% for $C_{p\,BEP}$, 0.6% for $C_{p\,HL}$ and 0.0002% for V. The close fit confirms a high trend-capturing accuracy of the response surfaces.

An overview of the goodness-of-fit indicators R^2_{adj} and σ_e, obtained from both RSM_A and RSM_B are shown in Table 5.6. R^2_{adj} is close to 1 and σ_e close to 0, which are indicating a good fit. RSM_B shows improvement for both goodness-of-fit indicators, except for $C_{p\,HL}$.

	R^2_{adj}				σ_e			
	$C_{p\,PL}$	$C_{p\,BEP}$	$C_{p\,HL}$	V	$C_{p\,PL}$	$C_{p\,BEP}$	$C_{p\,HL}$	V
RSM_A	0.95148	0.98596	0.98886	0.99999	0.02234	0.00451	0.00471	0.00024
RSM_B	0.95959	0.98643	0.98859	0.99999	0.02166	0.00449	0.00472	0.00022

Table 5.6: Indicators for the RSMs goodness-of-fit. RSM_A denotes the response surfaces provided by the simulations results performed with 5 inflation layers in the elbow, and RSM_B defines the refined response surfaces where the additional design points with 10 inflation layers in the elbow is added. $R^2_{adj} = 1$ and $\sigma_e = 0$ indicate a perfect fit.

The error-residuals of simulated versus predicted objective values are displayed in Figure 5.2. Compared to the other objectives, a slightly higher residual error is observed for $C_{p\,PL}$, and a slightly lower residual error is observed for V.

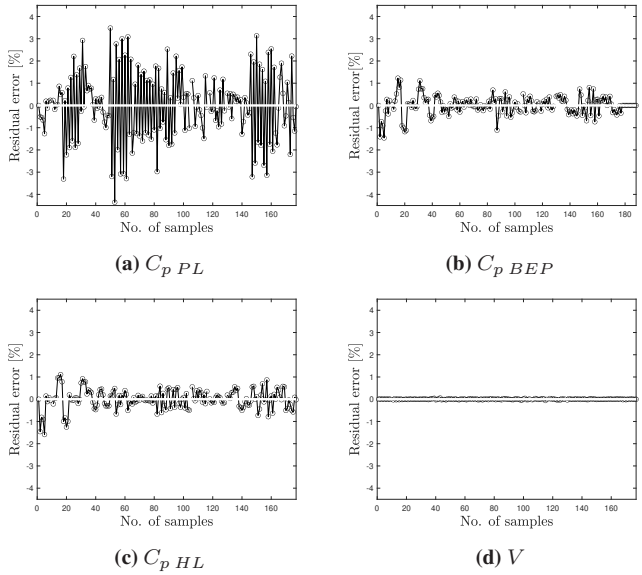

(a) $C_{p\,PL}$ **(b)** $C_{p\,BEP}$

(c) $C_{p\,HL}$ **(d)** V

Figure 5.2: Normalized residuals, defined as the difference between simulated and predicted value, divided by the simulated value for all response surfaces of RSM_B.

Sensitivity plots

The sensitivity of each objective centered around their CV is shown in Figure 5.3. The contours of each response surface are plotted by only letting one DV vary and the rest fixed at their CVs. This reflects general trends of how the objectives depend on each DV. Similar and conflicting behavior of how the objectives respond to changes in the same DV can be observed.

$C_{p\,PL}$ is most sensitive to changes in d_2, l_4 and l_5, whereas $C_{p\,BEP}$ and $C_{p\,HL}$ are most sensitive to l_4 and l_5. In general, $C_{p\,BEP}$ and $C_{p\,HL}$ contours look similar, indicating that these objectives correlating for the same DT designs. V is seen to be most sensitive to L and increase for all variables, except l_1 and r_1.

The contour of d_2 obtains a maximum value slightly above its center value for C_p at all OPs. This observation is most apparent at PL. The contours of h_1 and L show contradicting behaviour for C_p and V. V increases with h_1 and L, whereas C_p decreases for all OPs. However, $C_{p\,HL}$ is seen to decrease for both high and low values of h_1. All objectives increase with l_4 and l_5 and are seen to be very sensitive to them.

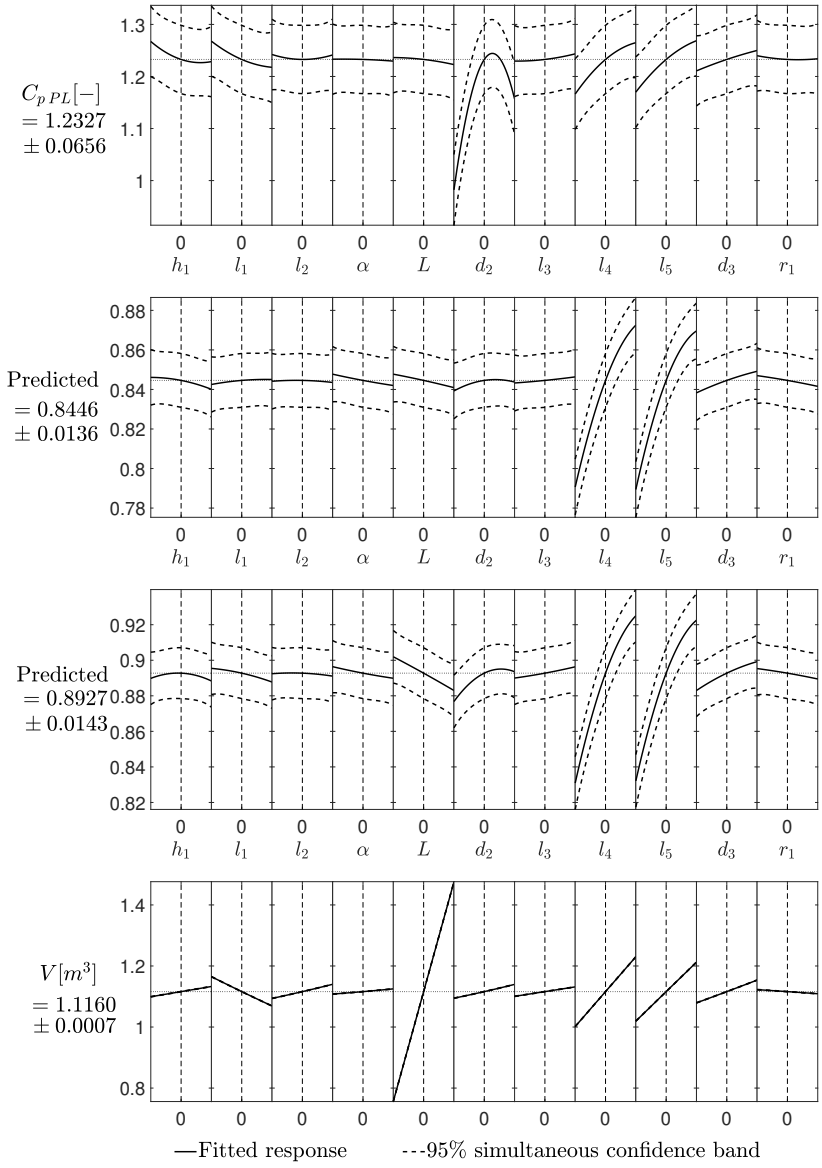

Figure 5.3: One-dimensional contours of the 11-dimensional RSMs showing the parameter sensitivity at the center point. Different parameters have different, and sometimes contradictory, effect on the DT optimization objectives.

5.3.4 Design exploration

100M random, distributed DT designs are generated uniformly within the design space. The designs are then evaluated by RSMs for each of the four objectives. Out of this population, 32.6M showed improvement in $C_{p\,PL}$, 45.3M showed improvement in $C_{p\,BEP}$, 42.8M showed improvement in $C_{p\,HL}$, and 51.2M showed improvement in V. Further more, the maximum improvement of each objective, separately, is found to be 12.62% in $C_{p\,PL}$, 5.38% in $C_{p\,BEP}$, 6.64% in $C_{p\,HL}$, and 46.52 % in V.

Figure 5.4, Figure 5.5, and Figure 5.6 show C_p plotted against V for each of the OPs. The objectives are normalized by their respective improvements over PS_{ref}. That is, all potentially improved designs lie in the 4th quadrant, where $C_p/C_{p\,ref} > 1$ and $V/V_{ref} < 1$. Out of the 100M predicted responses, 14.2M designs showed improvements of both C_p and V at PL, 19.1M at BEP, and 19.1M at HL.

For all OPs, an outer edge of the modeled responses becomes present in the 4th quadrant, relative the reference design as an origin. This contour indicates the maximum possible improvement for each pair of objectives plotted simultaneously, and is referred to as a Pareto Front. A design located at the Pareto Front is said to be Pareto optimal, and characterized by that any further improvement of one objective is impossible without worsening another.

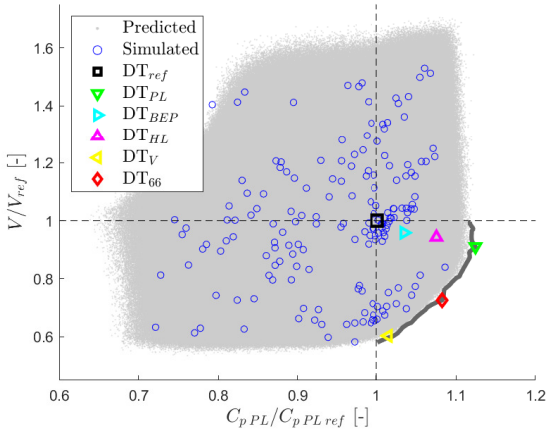

Figure 5.4: Comparison between the optimization objectives $C_{p\,PL}$ and V. 100M random designs are predicted and normalized by the objective value of the reference design. 14.2M of these designs show improvements in both objectives, and are located in the 4th quadrant, relative the reference design as the origin.

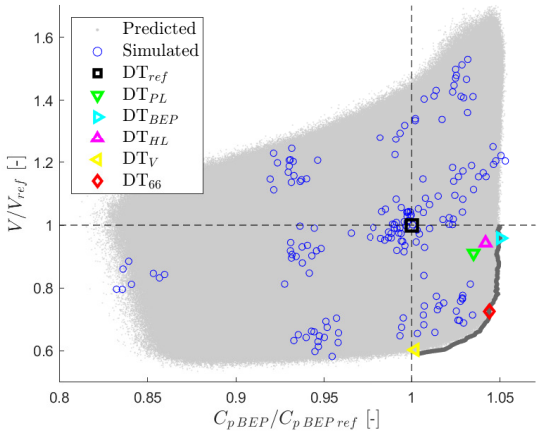

Figure 5.5: Comparison between the optimization objectives $C_{p\,BEP}$ and V. 100M random designs are predicted and normalized by the objective value of the reference design. 19.1M of these designs show improvements in both objectives, and are located in the 4th quadrant, relative the reference design as the origin.

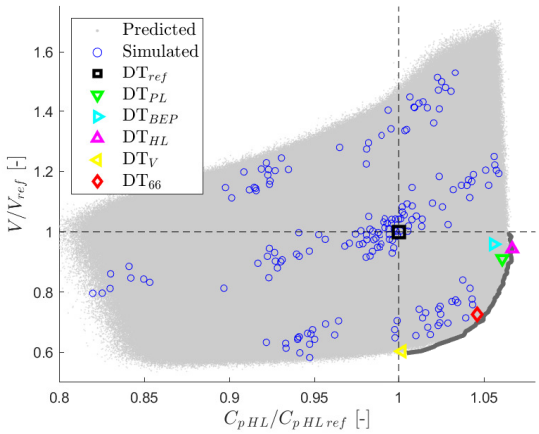

Figure 5.6: Comparison between the optimization objectives $C_{p\,HL}$ and V. 100M random designs are predicted and normalized by the objective value of the reference design. 19.1M of these designs show improvements in both objectives, and are located in the 4th quadrant, relative the reference design as the origin.

Search for optimized designs

The modeled responses are sorted into a population of predicted improved DT designs, referred to as Predicted Improved Modeled Population (PIMP). The designs in PIMP all have equal or better performance than PS_{ref} across all four objectives. Out of the 100M modeled responses, 10.2M designs showed the potential of being better than DT_{ref}.

Among PIMP, the maximum possible improvement for each objective is found to be 12.4% in $C_{p\,PL}$, 5.0% in $C_{p\,BEP}$, 6.6% in $C_{p\,HL}$, and 39.7% in V. The designs that maximize the improvement in each of the objectives, are, respectively, denoted DT_{PL}, DT_{BEP}, DT_{HL} and DT_{V}. Each of these designs favors improvement of only one objective, while at the same time making sure that the remaining objectives are at least as good as the reference.

A design that considers improvements for all four objectives simultaneously is also found by filtering the designs in PIMP. The design is found by letting d define the fraction of how much the objectives should be improved in their range from their value at PS_{ref} to their maximum value in PIMP. Then PIMP is filtered by several searches of gradually increased d until only one design is left. This design is found for $d = 0.66$ and referred to as DT_{66}. The design is predicted to give 8.3% improvement in $C_{p\,PL}$, 4.4% improvement in $C_{p\,BEP}$, 4.6% improvement in $C_{p\,HL}$ and 27.4% improvement in V.

The predicted performance of the suggested improved designs are plotted in Figure 5.4, Figure 5.5, and Figure 5.6. The designs located close to the Pareto Front indicate them to be Pareto optimal in the objectives plotted.

Finally, the predictions of the suggested improved designs are verified against PS and FS. The settings of the simulations are the same as for all previous simulations, defined in subsection 4.6.3, except that the general mesh algorithm was found to not work for DT_{66} in the elbow. Thus, a few more elements had to be added, and the order of meshing segments was changed for the elbow. The mesh settings of DT_{66} are presented in Appendix C. Table 5.7 shows the GPs of the candidates of improved DT designs described above and Figure 5.7 illustrates their geometries.

GP	$h_1[mm]$	$l_1[mm]$	$l_2[mm]$	$\alpha[^\circ]$	$L[mm]$	$d_2[mm]$	$l_3[mm]$	$l_4[mm]$	$l_5[mm]$	$d_3[mm]$	$r_1[mm]$
$\mathbf{DT}_{ref}$	477	1459	761	15.0	4374	404	277	636	588	308	160
$\mathbf{DT}_{PL}$	602	1058	975	15.2	3078	418	287	720	694	322	169
$\mathbf{DT}_{BEP}$	617	1864	950	13.1	3641	441	273	733	683	322	149
$\mathbf{DT}_{HL}$	592	1025	923	13.9	3135	441	286	745	678	322	152
$\mathbf{DT}_{V}$	335	1874	533	13.5	3100	400	279	563	684	296	175
$\mathbf{DT}_{66}$	335	1827	974	13.6	3065	407	265	710	662	323	176

Table 5.7: GPs comparison between DT_{ref} and candidates of optimized designs.

		$\mathbf{DT}_{PL}$	$\mathbf{DT}_{BEP}$	$\mathbf{DT}_{HL}$	$\mathbf{DT}_{V}$	$\mathbf{DT}_{66}$	$\mathbf{DT}_{ref}$
$C_{p\,PL}[-]$	Predicted	1.3863	1.2758	1.3259	1.2514	1.3351	1.2327
	PS$_i$ w/BC$_{ref}$	1.3503	1.2739	1.2975	1.2569	1.2733	1.2327
	FS$_i$	1.5179	1.4519	1.5445	1.4104	1.5184	1.4330
	PS$_i$ w/BC$_i$	1.3348	1.2542	1.2982	1.2387	1.2654	
$C_{p\,BEP}[-]$	Predicted	0.8742	0.8870	0.8799	0.8462	0.8817	0.8446
	PS$_i$ w/BC$_{ref}$	0.8789	0.8863	0.8824	0.8415	0.8786	0.8446
	FS$_i$	0.8990	0.9105	0.9046	0.8633	0.8997	0.8639
	PS w/BC$_i$	0.8794	0.8913	0.8855	0.8485	0.8860	
$C_{p\,HL}[-]$	Predicted	0.9468	0.9422	0.9520	0.8944	0.9339	0.8927
	PS$_i$ w/BC$_{ref}$	0.9550	0.9573	0.9546	0.9045	0.9290	0.8927
	FS$_i$	0.9792	0.9744	0.9731	0.9190	0.9483	0.9058
	PS$_i$ w/BC$_i$	0.9539	0.9542	0.9548	0.9056	0.9314	
$V[m^3]$	Predicted	1.0163	1.0699	1.0527	0.6731	0.8103	1.1160
	Simulated	1.0122	1.0668	1.0501	0.6776	0.8083	1.1160

Table 5.8: Comparison of predicted and simulated objective results between the suggested designs and the reference design.

An overview of the prediction and simulation of the suggested improved designs are displayed in Table 5.8. Whereas optimization-simulations are performed as PS, the prediction values should be compared against PS. FS of the suggested designs confirms the findings from the DT inlet BC test; that C_p is under-predicted for PSs. The percentage changes of simulation results between the suggested designs and the reference design are displayed in Table 5.9. The results verify improvements in the objectives of the suggested designs, despite FSs of DT_V, which obtain reduced C_p at BEP and PL.

		$\mathbf{DT}_{PL}$	$\mathbf{DT}_{BEP}$	$\mathbf{DT}_{HL}$	$\mathbf{DT}_{V}$	$\mathbf{DT}_{66}$
$C_{p\,PL}$	FS [%]	5.92	1.32	7.78	-1.58	5.96
	PS [%]	8.28	1.74	5.31	0.49	2.65
$C_{p\,BEP}$	FS [%]	4.06	5.34	4.71	-0.07	4.14
	PS [%]	4.12	5.53	4.84	0.46	4.90
$C_{p\,HL}$	FS [%]	8.10	7.57	7.43	1.46	4.69
	PS [%]	6.86	6.89	6.96	1.45	4.34
V	[%]	-9.30	-4.41	-5.91	-39.28	-27.57

Table 5.9: Percentage change in the objectives of the suggested designs relative to the reference design.

(a) DT_{ref}

(b) DT_{PL}

(c) DT_{BEP}

(d) DT_{HL}

(e) DT_{V}

(f) DT_{66}

Figure 5.7: Illustrations of the reference design and the suggested improved designs.

Chapter VI

Discussion

■ This chapter discusses the findings of the research. The first section discusses general trends observed from the response surfaces and evaluates the suggested improved designs. The second section discusses the different uncertainties of the analysis.

6.1 Finding an optimized design

Out of the 100M predicted responses, 10.2M designs yielded better performance across all four objectives, suggesting the existence of improved designs. Simulation results of the suggested improved designs show a close correlation between predicted and simulated responses, and DT with better performance in the objectives were confirmed by CFD.

6.1.1 Trends of the response surface

From Figure 5.3, the sensitivity of the objective to changes in each variable can be observed separately. The DVs of highest importance are identified by considering the variation in the objectives. It should be emphasized that the design space limits the indications of the most essential DVs. Thus if the design space was changed for some DVs, the observations might be different. The optimal range of each DV can also be discussed by considering the gradient of the contours. However, since only one DV is varied for each plot, trends can only be indicated. Since the response surfaces are functions of 11 DVs, their actual response is more complicated when allowing variations in all variables simultaneously.

The diameter of the cone outlet is described by d_2. Its contours obtain a maximum

value slightly above its center value for C_p at all OPs, but the observation is most apparent at PL. It indicates that d_2 should be increased slightly from its reference value to achieve maximum pressure recovery. Thus, high d_2 would give a more diverging cone, which can achieve higher pressure recovery. However, if the outlet diameter of the cone is increased too much, flow separation from the wall may occur. The maximum value of C_p close to the center value of d_2 indicates that the reference cone is close to optimal. It should be noted that h_1, denoting the cone length, is kept constant for these observations. Since the divergence of the cone is also dependent on h_1, maximum pressure recovery would probably be indicated for other d_2 values if h_1 is changed.

Increased C_p for PL and BEP combined with reduced V are indicated by reducing h_1. However, Figure 5.3 indicates that h_1 should be maintained around its CV to optimize C_p at HL. Again, it should be emphasized that pressure recovery in the cone is also highly dependent on d_2. Thus, the entire picture might not be reflected from the one variable contours.

The DT volume will intuitively increase with larger geometric dimensions. Surprisingly, l_1 and r_1 are shown to decrease V for higher values in Figure 5.3. This can be explained by the DTs' design constraints and the nature of the sensitivity plots. l_1 describes the horizontal length of the DT volume, whereas L describes the entire horizontal length of the DT. In the sensitivity plots, only one DV changed, whereas the others are held fixed. Thus, increasing l_1 and keeping L fixed increase the horizontal length of the elbow, as the horizontal length of the exit diffuser decreases. Since the cross-sectional area is higher in the exit diffuser than in the elbow, this reduces the entire DT volume. r_1 is describing the bowed corners of the DT outlet. Thus, increasing r_1 will lead to a decreased DT volume.

l_4 and l_5, which describe the height and width dimensions of the DT outlet, are shown to be crucial for all objectives. However, both C_p and V are increased for higher values of these dimensions. Since a higher C_p, and lower V is desired, the objectives must be balanced when configuring these parameters.

A contradicting behavior is observed in the contour plots of L. Intuitively, V increases with the horizontal length of the DT. In contrast, C_p appears to decrease for higher values of L. Thus, an optimal design is shown to be obtained for lower values of L. This observation is found by keeping the horizontal length of the elbow, l_1, constant. This indicates that designs with an increased horizontal length ratio of the elbow, relative to the exit diffuser, may be more optimal.

The observations from the sensitivity plots could be utilized for adjustments of the design space. E.g., the vertical length of the elbow l_2 and r_1 show less influence over the objectives, relative to the other variables. Thus, more limited optimization

could be done by excluding these variables from the analysis. Small changes in the contours may also indicate that the design space is too small for the given parameter.

6.1.2 Evaluation of the suggested designs

An optimized DT design is not unambiguous as several objectives are considered for the analysis. Depending on how the objectives are weighted relative to each other, various optimized designs can be found. E.g., if a hydropower plant is assumed to operate more at PL than HL, $C_{p\,PL}$ should be weighted more than $C_{p\,HL}$.

An optimized draft tube have been suggested for each objective which separately maximize one objective without worsening the others relative to the reference design. Additionally, DT_{66} was suggested as a design that optimize for a weighted sum of all four objectives. The suggested designs are found by filtration and maximum search in PIMP. Other improved designs can be found by considering other search criteria. For example, a more specific weighting of improvement in each objective could be emphasized.

The GPs of each suggested design is presented in Table 5.7, and their resulting geometries can be seen in Figure 5.7.

Some general trends are found from the GPs of the suggested improved designs. The horizontal length L of the DT is decreased, and the width of the outlet l_5 is increased for all designs. Increased performance from decreasing L was indicated by the sensitivity plot in Figure 5.3 and discussed in subsection 6.1.1. Increasing l_5 was also found to be important for higher C_p. All suggested designs, except DT_V, are found to have increased outlet diameter of the cone d_2, vertical length of the elbow l_2, and diameter of the elbow outlet d_3. For these designs, the values of d_3 is approximately equal to the upper limit of the design space, which may indicate that even better designs can be attainable for higher values of d_3.

Table 5.9 shows that all suggested designs had improvements in all objectives, except DT_V. FSs of PL and BEP are seen to decrease C_p relative the reference design. The reduction equals 1.58% for PL and 0.07% for BEP. Thus, if the goal is to find a DT with reduced V and no worsening in C_p, another design should be considered.

Simulation results of DT_{BEP} confirm that this design obtains highest improvement for C_p at BEP. Thus, if optimizing BEP is desirable, DT_{BEP} is a valid candidate.

DT_{PL} was predicted to give the highest value of C_p at PL among the suggested designs, but FS of DT_{HL} and DT_{66} gave higher values of C_p at PL. DT_{HL} was

analogously predicted to give the highest value of C_p at HL. However, FS of DT_{PL} and DT_{BEP} obtained the highest values of C_p at HL. Despite that, both DT_{PL} and DT_{HL} are verified to both give relative high improvement in C_p at both PL and HL, making them a good choice if improving the hydropower plant at off-design operating conditions is of most importance.

DT_{66} was chosen so that it improves all objectives simultaneously. The performance of the design is predicted to be located close to the Pareto front, in Figure 5.4, Figure 5.5, and Figure 5.6, indicating a Pareto optimal design. Simulation results confirms that the design obtains substantial improvements across all four objectives. DT_{66} also achieves notably better reduction in V, compared to the DT designs favoring improvements in C_p. Thus, if improvements in all objectives are desirable, DT_{66} is a strong candidate.

It should be noted that the values of all objectives predicted and simulated, are listed with four decimals in Table 5.8. By considering the uncertainty further discussed in section 6.2, the number of decimals might reflect a higher accuracy than the uncertainty allows.

6.2 Uncertainty and errors

Understanding possible sources of errors are essential for relating uncertainty to the results. In general, the simulations and RSM split the errors into two main categories. The hierarchy of simulation errors from highest to lowest is modeling errors, discretization errors, and iteration errors. However, a clear separation between the different categories does not exits, as e.g., modeling errors may influence the numerical errors. The same intricate relationship also exists between the errors in the simulations and the RSM, as poor simulation results may increase the uncertainty of the RSM.

6.2.1 Mesh evaluation

The quality of the mesh affects the accuracy of the simulations. The shape and size of elements, the resolution of cells close to the wall, and the GCI analysis are utilized to evaluate uncertainties and errors related to the mesh.

Boundary layer modeling

Table 5.1 lists the y^+ values obtained from the simulations. The averaged values are within the recommended range, ensuring that the first node is placed within the logarithmic region of the turbulent BL.

No evaluation of the y^+ values of the GV and runner blades are reported in this

thesis, but a previous evaluation of the mesh is presented by Iliev [11]. The quality of these meshes was assumed to be sufficient, without any further investigation. However, this does not exclude the GVs and the runner as potential sources of errors.

The minimum values of y^+ are found to be below the recommended limit of 30. As stated in subsection 2.2.6, the logarithmic BL is assumed to start around $y^+ = 30$. $y^+ > 11.6$ defines the lower bound of the buffer region, where the logarithmic relation is assumed to model the flow better than the linear relation in the viscous sub-layer. All minimum values of y^+ are found to be above 11.6, indicating no placement of nodes within the viscous sublayer. However, increasing the first layer thickness of the node might help to increase the minimum values of y^+ further.

The maximum values of y^+ for the mesh with 5 inflation layers in the elbow are in the range of about 200-300. High values like these may be an indication of the first node being placed far out in the logarithmic region of the BL, or in the worst case, outside of it. This may lead to a non-physical high thickness of the BL.

The average, minimum, and maximum values of y^+ are decreased when increasing the number of inflation layers in the elbow. The first layer thickness of the inflation layers is constant, independent of the number of inflation layers in the elbow. As seen in section subsection 2.2.6, y^+ is a function of the first nodal placement close to the wall, kinematic viscosity, and the friction velocity. Since the former two are constant across the two approaches, the discrepancy must be attributed to the latter. This indicates that the friction velocity and the wall shear stress is modeled differently when the number of inflation layers in the elbow is changed. In general, the simulations performed with 10 inflation layers in the elbow result in more acceptable y^+ values. This may indicate that the simulation performed with 10 inflation layers, undulating matters are more accurate. Considering the y^+ values obtained and the upper limit of the logarithmic region $y^+ \sim 200 - 300$, ANSYS' recommendation of having 10 nodes in the logarithmic region is likely not achieved, which in turn may lead to poor modeling of the BL. Reducing the growth rate factor of the inflation layers may overcome this issue.

Correct modeling of the BL is crucial to obtain correct values of the shear stress and viscous losses. This will affect the calculation of pressure losses and be essential for finding C_p. It should be noted that by using a wall function, the flow is not simulated, but modeled for the inner part of the wall BL. This may result in modeling errors, despite having y^+ values within the acceptable limits.

Mesh element quality

According to the mesh metrics listed in Table 5.2, the averaged values are within the recommended limits. However, the minimum values of the orthogonality angle of the mesh with 5 inflation layers, and the maximum volume expansion for both 5 and 10 inflation layers, are outside the recommended limits. This indicates that both meshes used in the simulations contained some elements of poor quality.

Both values for orthogonality angels and volume expansion are outside the recommended range. Mesh elements with these values are potential sources of discretization errors. Since the averaged values are within the acceptable limits, most elements are assumed to have sufficient quality. However, the elliptic nature of the governing equations might lead to a propagation of discretization error from the poor mesh elements.

Ansys Mechanical rates the averaged mesh quality as 60%, where 100% is ideal. The exact consequence of this rating is unclear, but it suggests that it is possible to obtain higher quality meshes. The worst performing mesh element has a quality of 2%, highlighting the variation of mesh quality among the elements.

The number of elements and nodes affects the simulation time. Thus, increasing the mesh resolution for better accuracy must be traded off for a longer computational time. An unstructured mesh is utilized for the optimization study, but instead, considering a structured mesh, computational time may be decreased as information is stored more efficiently. Additionally, more efficiently solvers exist for structured meshes.

GCI analysis

The results of the GCI analysis presented in Table 5.3, show considerable larger GCI for PL compared to BEP and HL. In general, a low GCI value indicates a well-converged result that is close to grid-independent.

A possible cause of the high GCI value obtained for PL might be the observed oscillation. The calculated values of C_p are lower for both the fine and the coarse meshes, compared to the medium resolution mesh. The oscillation can indicate instabilities, which makes it impossible to find a converged solution. A possible source of this issue may be that the simulation is badly posed with the BCs. Thus, performing the GCI study on an FS might give a lower GCI value.

For the optimization simulations in this work, the medium resolution mesh is utilized. The GCI_{medium} values emphasize that numerical uncertainty is likely present in the results.

6.2.2 Draft tube inlet boundary condition evaluation

As seen in DT inlet BC test 1, there is a difference in C_p calculated from FS_i and PS_i. However, Figure 5.1 indicates that when modeling C_p along the meridian distance of the DT, both FS and PS appear to follow the same trends. For all designs and all OPs, FS_i predicts C_p to be higher than PS_i. The biggest difference between FS and PS is observed around the inlet region, indicating that the inlet BC for PS causing modeling errors.

PL was found to result in a larger difference in C_p compared to the two other OPs. HL had a slightly smaller difference in C_p compared to BEP, indicating that the difference in C_p between FS_i and PS_i is less for higher discharge. A possible explanation could be that C_p is defined, as seen in Equation 4.1, with the discharge in the denominator. Thus, modeling errors of the flow field introduced by excluding the GVs and the runner are not necessarily smaller at higher loads. However, with respect to C_p, the differences between FS_i and PS_i are found to be smaller for higher loads.

According to the results from DT inlet BC test 2, there is a difference in C_p calculated when PS is performed with different BCs. In contrast to test 1, the absolute differences in C_p decrease for lower discharge. **??** highlights that C_p does not follow the same trend along the DTs meridian line for the different simulations. However, the data presented in Table 5.4 indicate that the absolute difference observed for C_p is less than 1%. Thus using BC_{ref} for all PS in the optimization should be a sufficient approximation.

In Table 5.4 it can be seen that $\epsilon^{(1)} > \epsilon^{(2)}$. This indicates that values of C_p obtained from simulations are more sensitive to the presence of the GV and runner than to the BC imposed on the PS.

The DT inlet BC tests were only conducted on three different DT designs. Thus, it is impossible to quantify potential modeling errors introduced by removing the GVs and runner from the simulations. However, the magnitude of the errors observed at different OPs were of comparable size for all DTs. This indicates that some general trends are captured from the test results.

Simulation results of the suggested designs, strengthen the findings from the DT inlet BC tests. Table 5.8 shows that FS gives higher C_p values than PS. Also, comparing PS_i with BC_{ref} and PS_i with BC_i indicate a small difference in C_p.

The DT inlet BC tests investigate modeling errors introduced by excluding the GVs and the runner from the simulations. Despite the modeling errors introduced by fixing the velocity profile at the DT inlet, improved DT designs are found.

6.2.3 Simulation assumptions

Simulation assumptions such as the choice of turbulence model, neglecting transient effects, and modeling the flow as single-phase might introduce modeling errors that must be considered.

Choosing a more sophisticated turbulence model than $k - \epsilon$, would model turbulence effects better. However, this would likely increase the computational time needed and require a significantly finer mesh. For instance, using the SST turbulence model without a wall function would require y^+ values below 1, requiring a very fine mesh close to the wall to solve the flow field in the viscous sublayer.

All simulations performed are steady-state, even though the flow in the DT is highly time-dependent. The transient effects of the rotating vortex rope at PL and the pulsating cavitation column at HL are, therefore, not considered. This might explain the larger errors found for PL in the GCI analysis and the DT inlet BC tests. This indicates that it might be impossible to force a steady solution of the rotating vortex rope.

The objective of the thesis was to consider the steady-state operating conditions of the turbine. Even though the rotational speed of the runner is fixed for each simulation, assuming the flow to be steady-state might be a debatable decision. However, performing all simulations as transient would increase the computational time substantially. One way to circumvent this would be to use transient simulations as an evaluation tool for a subset of the most promising candidates. This was initially part of the research plan but was omitted due to limited time.

The effects of cavitation are neglected from the simulations by not considering multi-phase flow. However, the consequences of cavitation are large, both locally in the DT, as well as for the entire hydropower plant. Thus, multi-phase simulations should also be considered to verify the suggested improved designs. A solution with smaller computational cost is to investigate low-pressure zones in single-phase simulations. If the pressure is found to be below the vapor pressure, cavitation is indicated.

6.2.4 Geometry scripting errors

Some DPs caused the geometry generation script to fail. Rerunning the script with the same parameters eventually succeeded, implying a problem related to multiprocessing or resource acquisition on the host system. This error caused some delay, but since the program eventually managed to finish successfully, the issue did not affect the correctness of the subsequent analysis. In the future, it may be useful to troubleshoot the script further to streamline the optimization process better.

6.2.5 Response Surface Modeling accuracy

Response surfaces were first built by the optimization simulations performed with only 5 inflation layers in the elbow, denoted RSM_A. The comparison of simulation results of DPs with 10 inflation layers in the elbow and their predicted responses with RSM_A shows a close fit. This indicates a high trend-capturing accuracy and confirms that RSMs may be a good surrogate model. This close fit also indicates that simulating most of the DPs with 5 inflation layers in the elbow does not cause a large difference.

The response surfaces were further refined with the updated DPs as RSM_B, which were utilized for further optimization. RSM_B was built with 4 DPs excluded due to meshing algorithm failure. There was no time for considering different meshing algorithms that could potentially work for all DPs. The optimization problem is overdetermined, meaning that the number of samples is higher than the number of regression coefficients. Thus, the response surfaces could be built without the failed DPs. However, it will have caused a decrease in the accuracy of the RSM.

The goodness-of-fit indicators for both RSM_A and RSM_B are shown in Table 5.6. R^2_{adj} is close to 1, and σ_e is close to 0 for all the response surfaces, indicating a good fit. The refined response surfaces show improvement in all objectives, except $C_{p\,HL}$, which is slightly worsened.

The residual error is the sampled versus predicted responses of the objectives are shown in Figure 5.2. It can be observed that the uncertainty for the response surfaces is highest for $C_{p\,PL}$ and lowest for V. The response surfaces of $C_{p\,BEP}$ and $C_{p\,HL}$ were shown to have approximately the same uncertainty.

The higher uncertainty for $C_{p\,PL}$ may be a result of the generally higher uncertainty found for simulating this OP compared to BEP and HL. The relatively low uncertainty found for V is most likely caused by the fact that V is a purely geometric problem. V is calculated from the aggregate volume of all mesh elements and is thus not affected by simulation errors.

Uncertainty from the simulations propagates further into the RSM. Thus the accuracy of the response surfaces may be improved by improving simulation fidelity. However, there may be an upper limit of how much the response surfaces can be improved. The responses of the objectives might not fit a second-order response surface perfectly, independent of simulation quality. Thus, other surrogate models may be worth considering. However, it must be stressed that the overall goal of the optimization is not to achieve highly accurate results but to capture the most important trends.

A strong correlation between predicted and simulated responses of the suggested designs can be seen in Table 5.8. This confirms that the RSM works for finding better designs. As the optimization simulations were performed as PS, predicted responses must be compared against the PS values.

FSs of the suggested designs result in higher C_p values compared to PS. This strengthens the findings of the DT inlet BC tests. The response surfaces do not capture the difference between PS and FS. As the FS gives more realistic pictures of the flow condition in the DT, a possible improvement of the RSM may be to utilize FS rather than PS for the optimization simulations. A less computationally expensive improvement may be to decrease the modeling error of PS, by considering another BC at the inlet.

Chapter VII

Conclusion

■ This chapter concludes the research carried out. The first section summarizes the key findings, and the other section discuss ideas for further work.

7.1 Key findings

The purpose of this thesis has been to optimize a draft tube design for a variable speed operating Francis turbine. An optimal design was discussed in terms of increased pressure recovery and decreased volume, relative to a reference design. Three operation points corresponding to part load, best efficiency point, and high load, were considered for the analysis. Four optimization objectives were built with response surface modeling and utilized to predict the pressure recovery at the different operation points, and the draft tube volume.

From $100 \cdot 10^6$ predicted responses, $10.2 \cdot 10^6$ designs were found to give improved performance across all four objectives simultaneously. Five optimized designs were proposed; the first four corresponding to designs with the highest given score for a single objective, while simultaneously avoiding any reduction in performance for the other objectives compared to the reference. The last proposed design was selected by considering simultaneous improvement across all four objectives.

Common among the suggested designs was a reduction in the horizontal length of the draft tube. Additionally, all designs, except the one favoring decreased volume, were found to have the diameter of the elbow outlet close to the upper limit of the design space. This indicates that even better designs might be found by extending the limits of this value.

The simulations were performed with a velocity boundary condition at the draft tube inlet exported from a simulation of guide vanes, runner, and the reference draft tube. The effect of excluding the guide vanes and the runner from the simulations indicated that the pressure recovery would be under-predicted by simulating only the draft tube. This result was further confirmed by simulations of the predicted improved designs, including the guide vanes and the runner.

An error in the mesh setup caused most of the design points to be simulated with five inflation layers in the elbow. This may have caused the viscous losses, and the shear stresses in the turbulent boundary layer to be modeled incorrectly. Response surfaces were first built by the results obtained from the design points simulated with too few inflation layers in the elbow. Predictions of these response surfaces, compared to design points simulated with ten inflation layers in the elbow, showed a close fit. This indicates that potential modeling errors, introduced by simulating most of the designs with too few inflation layers, are unlikely to have affected the analysis.

Results from part load were subject to a higher uncertainty than the results from the other operating points. A possible explanation was that part load operation of a turbine gives rise to a highly transient flow in the draft tube. Thus, modeling the flow in the draft tube as steady-state may introduce significant modeling errors.

The choice of turbulence model and assumptions of steady-state and single-phase flow may introduce modeling errors. The mesh and choice of discretization schemes give rise to discretization errors. Iteration errors due to not fully converged simulations may also be a source of concern. However, the results from the research should be valid when performing a relativistic comparison of the performance.

Response surfaces were built with high accuracy, as indicated by the goodness-of-fit scores. The predicted responses of the suggested designs were verified against simulations. The results showed a close fit between the predicted and simulated objectives, demonstrating that the optimization method works.

Simulation results of the design favoring decreased volume showed small reductions in the pressure recovery at part load and best efficiency point. Thus, this design should not be considered optimal, unless a reduction of the volume is of higher importance than the associated worsening in pressure recovery. The simulation results of the other suggested designs showed improvements for all optimization objectives. Thus, all these designs can be suggested as improvements. The ultimate choice of design depends on which operating points it is most important to improve, and civil costs, which may constrain the draft tube volume.

7.2 Further work

The accuracy of the analysis may be improved in several ways. By reducing simulation error, the response surface models' fidelity may be improved.

Modeling errors may be reduced by considering other boundary conditions. For instance, total pressure and velocity direction could be specified at the draft tube inlet and mass flow rate at the outlet. Performing the entire optimization with guide vanes and the runner is another, more computational expensive suggestion. Choosing a more sophisticated turbulence model will capture turbulence effects better, and considering transient simulations may reduce the high uncertainty observed when operating at part load. Discretization error may be reduced by rerunning the simulations with an inflation layer setup that models the turbulent boundary layer better. Additionally, a higher quality mesh may be considered.

Increasing the limits of the design variables that were indicated to be too small, could potentially lead to even better designs. The optimization study can also be repeated with only the design variables that the response surfaces were the most sensitive to. That way, the analysis will only consider the parameters of the highest importance. Additionally, it may be possible to achieve a better approximation by exploring different types of surrogate models.

The proposed designs should be verified against simulations with higher accuracy. If these simulations confirm the improvements, a natural next step would be to validate the findings with physical prototype testing.

This thesis was limited to consider improved draft tube performance in terms of increased pressure recovery and decreased volume. Other characteristics such as the energy loss coefficient, the draft tube efficiency, or the surface area of the draft tube may also be considered as objectives.

References

[1] Gogstad, P. J., "Experimental Investigation and Mitigation of Pressure Pulsations in Francis Turbines," .

[2] Mosonyi, E., *Water Power Development Low Head Power Plants*, 3rd ed., Akademiai Kiado.

[3] "ANSYS CFX 2020R1 Solver Theory Guide," accessed 2020-07-01, https://ansyshelp.ansys.com/Views/Secured/corp/v201/en/cfx_thry/cfx_thry.html

[4] Li, Q., Chen, W., Liu, S., and Fan, H., "Topology Optimization Design of Cast Parts Based on Virtual Temperature Method," **94**, pp. 28–40.

[5] Marjavaara, B. D., "CFD Driven Optimization of Hydraulic Turbine Draft Tubes Using Surrogate Models," .

[6] White, F. M., *Viscous Fluid Flow*, 3rd ed., McGraw Hill.

[7] Holstad, M., Ruen, I. R., and Billit, T. J., "Elektrisitet," accessed 2020-05-24, https://www.ssb.no/energi-og-industri/statistikker/elektrisitet/aar/2019-11-28

[8] "Francis Hydro Turbine | GE Renewable Energy," accessed 2020-05-24, https://www.ge.com/renewableenergy/hydro-power/large-hydropower-solutions/hydro-turbines/francis-turbine

[9] Øgaard, E., "Francis-turbin," accessed 2020-05-24, http://www.vasskrafta.no/turbinar/francis-turbin-article214-479.html

[10] Dnv-GL, "Energy Transition Outlook 2019," accessed 2020-05-24, https://eto.dnvgl.com/2019

[11] Iliev, I., Tengs, E. O., Trivedi, C., and Dahlhaug, O. G., "Optimization of Francis Turbines for Variable Speed Operation Using Surrogate Modeling Approach," .

[12] "HydroFlex," accessed 2020-05-24, https://www.h2020hydroflex.eu/

[13] "Francis-99 - NTNU," accessed 2020-05-24, https://www.ntnu.edu/nvks/francis-99

[14] Iliev, I., Trivedi, C., and Dahlhaug, O. G., "Variable-Speed Operation of Francis Turbines: A Review of the Perspectives and Challenges," **103**, pp. 109–121.

[15] Lyutov, A. E., Chirkov, D. V., Skorospelov, V. A., Turuk, P. A., and Cherny, S. G., "Coupled Multipoint Shape Optimization of Runner and Draft Tube of Hydraulic Turbines," **137**(11).

[16] Dörfler, P., Sick, M., and Coutu, A., *Flow-Induced Pulsation and Vibration in Hydroelectric Machinery: Engineer's Guidebook for Planning, Design and Troubleshooting*, Springer-Verlag.

[17] Gubin, M. F., *Draft Tubes of Hydro-Electric Stations*, Amerind Publishing Co.

[18] "ANSYS CFX 2020R1 Reference Guide," accessed 2020-07-01, https://ansyshelp.ansys.com/Views/Secured/corp/v201/en/cfx_ref/cfx_ref.html

[19] "ANSYS CFX 2020R1 Solver Modeling Guide," accessed 2020-07-01, https://ansyshelp.ansys.com/Views/Secured/corp/v201/en/cfx_mod/cfx_mod.html

[20] "ANSYS 2020R1Meshing User Guide," accessed 2020-07-01, https://ansyshelp.ansys.com/account/secured?returnurl=/Views/Secured/prod_page.html?pn=Meshing&prodver=20.1&lang=en

[21] "Top Computational Fluid Dynamics (CFD) Software: List, Reviews, Comparison & Price | TEC," accessed 2020-06-22, https://www3.technologyevaluation.com/sd/category/computational-fluid-dynamics-cfd

[22] Marjavaara, D. and Lundström, S., "Response Surface-based Shape Optimization of a Francis Draft Tube," **17**(1), pp. 34–45.

[23] McNabb, J., Devals, C., Kyriacou, S. A., Murry, N., and Mullins, B. F., "CFD Based Draft Tube Hydraulic Design Optimization," **22**(1), p. 012023.

[24] Klewicki, J. C., "Reynolds Number Dependence, Scaling, and Dynamics of Turbulent Boundary Layers," **132**(9).

[25] "Procedure for Estimation and Reporting of Uncertainty Due to Discretization in CFD Applications," **130**(7).

[26] Cavazzuti, M., *Optimization Methods: From Theory to Design*, Springer.

[27] Hazewinkel, M., *Bézier Curve*, Springer Science+Business Media B.V. / Kluwer Academic Publishers.

[28] Box, G. E. P. and Behnken, D. W., "Some New Three Level Designs for the Study of Quantitative Variables," **2**(4), pp. 455–475, 1266454.

[29] "ANSYS 2020R1 DesignXplorer User's Guide," accessed 2020-07-01, https://ansyshelp.ansys.com/account/secured?returnurl=/Views/Secured/corp/v201/en/wb_dx/dxbook.html

[30] Myers, R. H., Montgomery, D. C., and Anderson-Cook, C. M., *Response Surface Methodology*, 3rd ed., John Wiley & Sons, Inc.

[31] Çlabuk, H. and Modi, V., "Optimum Plane Diffusers in Laminar Flow," **237**, pp. 373–393.

[32] Madsen, J. I., *Design Otimization of Internal Flow Devices*.

[33] Mun, C. N., Ba, D. C., Yue, X. J., and Kim, M. I., "Multi-Objective Optimization of Draft Tube in Francis Turbine Using DOE, RBF and NSGA-II," .

[34] chol Nam, M., Dechun, B., Xiangji, Y., and Mingri, J., "Design Optimization of Hydraulic Turbine Draft Tube Based on CFD and DOE Method," **136**, p. 012019.

[35] Shojaeefard, M. H., Mirzaei, A., and Babaei, A., "Shape Optimization of Draft Tubes for Agnew Microhydro Turbines," **79**, pp. 681–689.

[36] Soni, V., Roghelia, A., Desai, J., and Chauhan, V., "Design Development of Optimum Draft Tube for High Head Francis Turbine Using CFD," *ResearchGate*, accessed 2020-04-07, https://www.researchgate.net/publication/262241778_DESIGN_DEVELOPMENT_OF_OPTIMUM_DRAFT_TUBE_FOR_HIGH_HEAD_FRANCIS_TURBINE_USING_CFD?channel=doi&linkId=0c9605371f4798cca1000000&showFulltext=true

[37] Breivik, S. R., “CFD Analysis of Flow in a Kaplan Turbine,” .

[38] Jost, D. and Lipej, A., “Numerical Prediction of Non-Cavitating and Cavitating Vortex Rope in a Francis Turbine Draft Tube,” **57**, pp. 445–456.

[39] Mauri, S., “Numerical Simulation and Flow Analysis of an Elbow Diffuser,” accessed 2020-06-07, https://www.researchgate.net/publication/311081993_Numerical_simulation_and_flow_analysis_of_an_elbow_diffuser

[40] Marjavaara, M. and Lundström, S., 2007, “Response surface-based shape optimization of a Francis draft tube,” **17**(1), pp. 34–35.

Appendix - A

The k-ϵ model

The empirical values and equations presented in this section are found from the ANSYS CFX 2020R1 Solver Theory Guide [3]. An overview of the default values ANSYS CFX utilize for the $k - \epsilon$ model is shown in Table A.1.

Constant	Value
C_μ	0.09
$C_{\epsilon 1}$	1.45
$C_{\epsilon 2}$	1.90
σ_k	1.00
σ_ϵ	1.30

Table A.1: Empircal constants default values of the $k - \epsilon$ model in ANSYS CFX

The turbulence production term P_k is modeled as:

$$P_k = \mu_t \left(\frac{\partial c_i}{\partial x_j} + \frac{\partial c_j}{\partial x_i} \right) \frac{\partial c_i}{\partial x_j} - \frac{2}{3} \frac{\partial c_k}{\partial x_k} \left(3\mu_t \frac{\partial c_k}{\partial x_k} + \rho k \right) \tag{A.1}$$

It reflects the turbulence production due to viscous forces. The second term does not contribute significantly to the production for incompressible flow as $\partial c_k / \partial x_k$ becomes small.

Equation 2.22 and Equation 2.22 presented in subsection 2.2.3, shows the transport equations of kinetic energy and turbulent dissipation rate without influence of buoyancy forces. If buoyancy forces also are considered, the buoyancy terms P_{kb} and $P_{\epsilon b}$ must be added to the transport equations and the buoyancy turbulence must be modeled as well.

Appendix - B

The GCI-method

A grid independent solution of a CFD simulation is desirable, meaning that the results should not change when the mesh is refined. Calculating the GCI value gives an indication of how much the solution would change with a further refinement of the mesh. The GCI value should be small to ensure that the computation is within the asymptotic range. This subsection lists the methods steps, as a more deeply description can be found in [25].

Step 1

Define a representative mesh size *h*.

$$h = \left[\frac{1}{N}\sum_{i=1}^{N}(\Delta V_i)\right]^{1/3} \tag{B.1}$$

where ΔV_i is the volume of the i^{th} mesh element and N is the total number of mesh elements.

Step 2

Select three different mesh resolutions, and run simulations to determine the objectives derived from key variables of the results. The objective(s) can i.e. be the pressure recovery factor or the energy loss coefficient defined in AUTOREF cp and AUTOref ELC. The objective of interest are refered to with the variable ϕ and the grid refinement factor between the different meshes are defined as $r = h_{coarse}/h_{fine}$. From experience it is desireble that $r > 1.3$.

Step 3

Calculate p, the apparent order of the method with the equations:

$$p = \frac{1}{ln(r_{21})} |ln|\epsilon_{32}/\epsilon_{21}| + q(p)| \tag{B.2}$$

$$q(p) = ln\left(\frac{r_{21}^p - s}{r_{32}^p - s}\right) \tag{B.3}$$

$$s = 1 \cdot (\epsilon_{32}/\epsilon_{21}) \tag{B.4}$$

where $h_1 < h_2 < h_3$, $r_{21} = h_2/h_1$, $r_{32} = h_3/h_2$, $\epsilon_{32} = \phi_3 - \phi_2$, $\epsilon_{21} = \phi_2 - \phi_1$

Step 4

Calculate the extrapolated objective values from:

$$\phi_{ext}^{21} = (r_{21}^p \phi_1 - \phi_2)/(r_{21}^p - 1) \tag{B.5}$$

Step 5

Calculate the error estimates of the approximate relative error (Equation B.6), extrapolated relative error (Equation B.7) and the fine-grid convergence index (Equation B.8.

$$e_a^{21} = \left|\frac{\phi_1 - \phi_2}{\phi_1}\right| \tag{B.6}$$

$$e_{ext}^{21} = \left|\frac{\phi_{ext}^{21} - \phi_2}{\phi_{ext}^{21}}\right| \tag{B.7}$$

$$GCI_{fine}^{21} = \frac{1.25 e_a^{21}}{r_{21}^p - 1} \tag{B.8}$$

Step 4 and 5 can also be done similar for calculating the numerical error for mesh 2, by switching index 1 to 2 and index 2 to 3. Notably, the GCI-index only reports numerical uncertainty and does not account for modeling errors.

Appendix - C

Mesh settings

The mesh setup of the GCI analysis and DT_{66} are presented in Table C.1 and Table C.2. The medium mesh setup of the GCI analysis is utilized for providing mesh for the optimization-simulations. An explanation of how the mesh is generated is given in section 4.4.

No.	**Method**	**SES**$[mm]$				**FLT**	**GR**				**Order**	
		C	M	F	DT_{66}	$[mm]$	C	M	F	DT_{66}	C/M/F	DT_{66}
1	PC	-	-	-	-	0.5	1.25	1.20	1.18	1.20	13	13
2	MZ	10.0	7.0	5.0	7.0	0.5	1.25	1.20	1.18	1.20	1	1
3	MZ	15.0	10.0	7.0	10.0	0.5	1.25	1.20	1.18	1.20	2	2
4	PC	-	-	-	-	ST	1.25	1.20	1.18	1.20	14	14
5	MZ	20.0	15.0	10.0	15.0	0.6	1.25	1.20	1.18	1.20	3	7
6	MZ	25.0	20.0	12.0	20.0	0.6	1.25	1.20	1.18	1.20	4	6
7	MZ	30.0	25.0	15.0	25.0	0.6	1.25	1.20	1.18	1.20	5	5
8	MZ	40.0	30.0	20.0	30.0	0.6	1.25	1.20	1.18	1.20	6	4
9	MZ	45.0	40.0	25.0	40.0	0.6	1.25	1.20	1.18	1.20	7	3
10	PC	-	-	-	-	ST	1.25	1.20	1.18	1.20	15	15
11	MZ	60.0	50.0	35.0	50.0	1.0	1.25	1.20	1.18	1.20	8	8
12	MZ	50.0	40.0	30.0	40.0	1.0	1.25	1.20	1.18	1.20	9	9
13	MZ	40.0	25.0	15.0	25.0	1.0	1.25	1.20	1.18	1.20	10	10
14	MZ	25.0	15.0	12.0	15.0	1.0	1.25	1.20	1.18	1.20	11	11
15	MZ	15.0	10.0	8.0	10.0	1.0	1.25	1.20	1.18	1.20	12	12

Table C.1: Mesh setup for the GCI analyse and DT_{66}. C, M and F denotes coarse, medium and fine meshes. PC = Patch Confoming Mesh method and MZ = Multizone mesh method. SES = Sweep Element Size of Multizone Mesh Method. FLT = First Layer Thickness of inflation layers, GR = Growth rate of inflation layers and ST = smooth transition of inflation layers. No. denotes the mesh segments, illustrated in Figure 2.8.

Interface	**Element size**$[mm]$			
	C	M	F	DT_{66}
Hub	5.0	2.0	1.5	2.0
Inlet	10.0	5.0	3.0	5.0
Cone	10.0	5.0	3.0	5.0
Elbow	16.0	15.0	12.0	10.0[1]
Exit Diffuser	25.0	20.0	12.0	20.0

Table C.2: Interface sizing setup for the GCI analyse and DT_{66}. C, M and F denotes coarse, medium and fine meshes. Interfaces are illustrated in Figure 2.8.
[1]The interface utilized for sizing in the elbow is the interface between segment 7 and 8, instead of the interface between segment 4 and 5.

Appendix - D

DT inlet BC tests

D.1 Test 1:

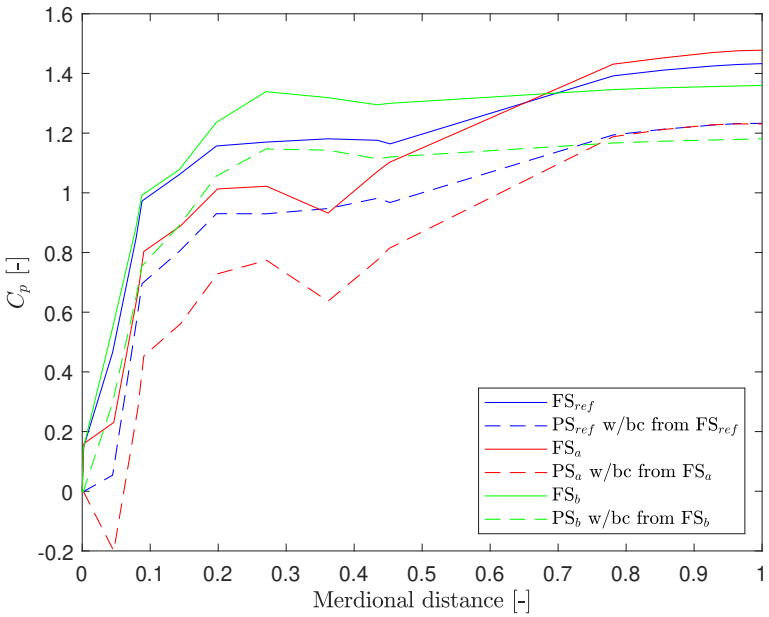

Figure D.1: PL comparison of C_p plotted as a function of merdional distance along DT for FS and PS.

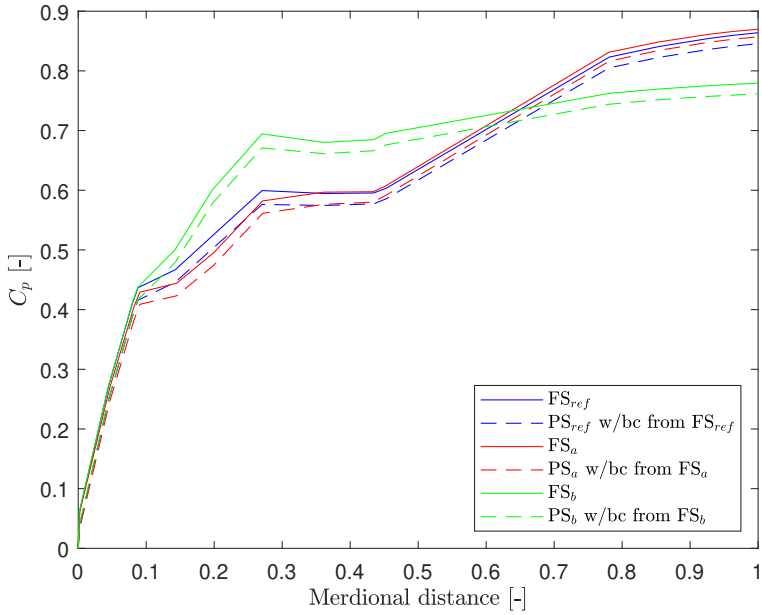

Figure D.2: BEP comparison of C_p plotted as a function of merdional distance along DT for FS and PS.

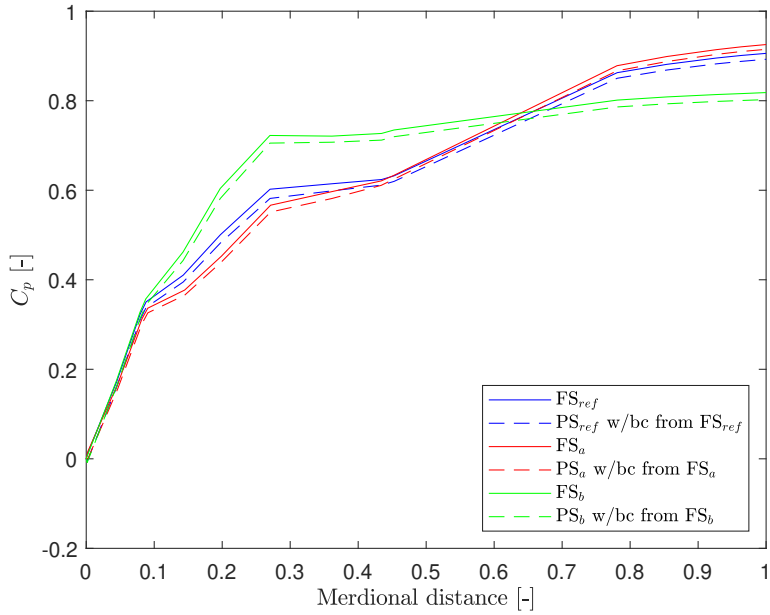

Figure D.3: HL comparison of C_p plotted as a function of merdional distance along DT for FS and PS.

D.2 Test 2:

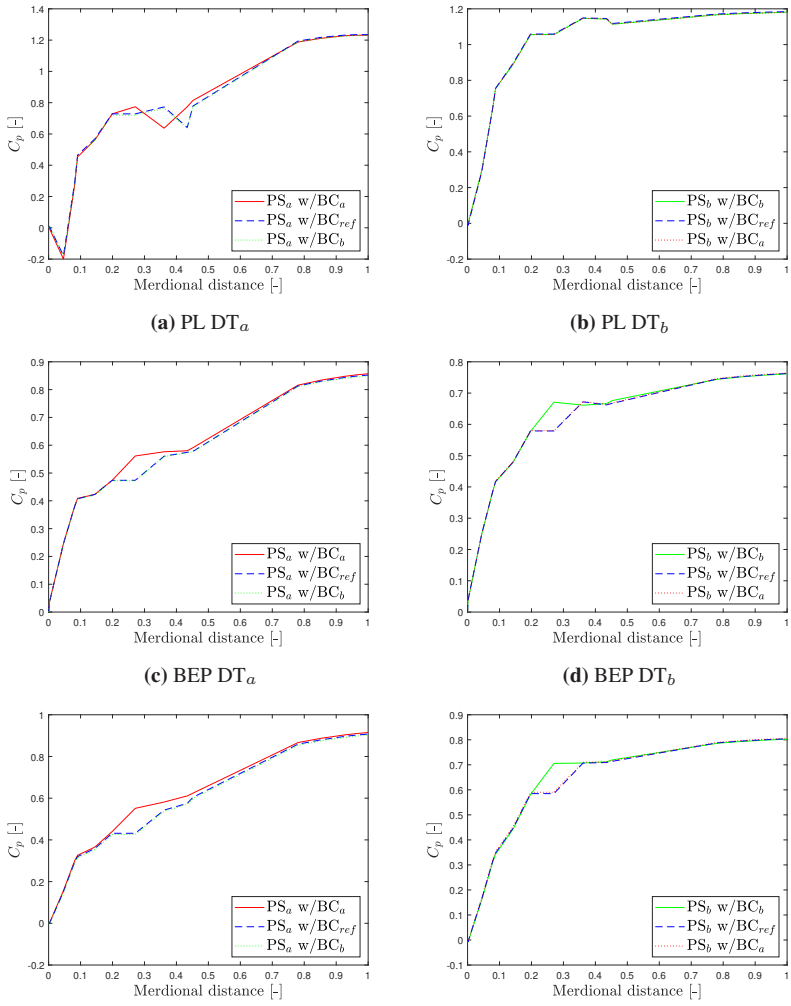

(a) PL DT$_a$ **(b)** PL DT$_b$

(c) BEP DT$_a$ **(d)** BEP DT$_b$

(e) HL DT$_a$ **(f)** HL DT$_b$

Figure D.4: C_p plotted along the merdional DT distance for DT inlet BC test 2 of design DT$_a$ and DT$_b$.

Appendix - E

Electronic attachments

The elctronic attachments of this thesis are organized in folders. The folder name and content is listed in Table E.1.

Folder	**Content**
Geometry	Python script of the geometry configuration
GCI	MATLAB script of the GCI calculations.
Optimization-Simulations	Ansys WB-projects of the simulations at different OPs.
	DT inlet BC velocity csv files
RSM	createRSMsRefined: MATLAB script for RSM
	searchOptimal: MATLAB script for searching optimal designs
	PLr.csv, BEPr.csv, HLr.csv: simulation result files

Table E.1: Overview of electronic attachments

Ingelin Herland

Design-Optimization of a Francis turbine draft tube

NTNU
Norwegian University of
Science and Technology